Fitting line projections in non-central catadioptric cameras with revolution symmetry

Jesus Bermudez-Cameo[a,**], Gonzalo Lopez-Nicolas[a], Jose J. Guerrero[a]

[a]Instituto de Investigación en Ingeniería de Aragón, Universidad de Zaragoza, C/ María de Luna 1, Zaragoza, 50018, Spain

ABSTRACT

Line-images in non-central cameras contain much richer information of the original 3D line than line projections in central cameras. The projection surface of a 3D line in most catadioptric non-central cameras is a ruled surface, encapsulating the complete information of the 3D line. The resulting line-image is a curve which contains the 4 degrees of freedom of the 3D line. That means a qualitative advantage with respect to the central case, although extracting this curve is quite difficult. In this paper, we focus on the analytical description of the line-images in non-central catadioptric systems with symmetry of revolution. As a direct application we present a method for automatic line-image extraction for conical and spherical calibrated catadioptric cameras. For designing this method we have analytically solved the metric distance from point to line-image for non-central catadioptric systems. We also propose a distance we call *effective baseline* measuring the quality of the reconstruction of a 3D line from the minimum number of rays. This measure is used to evaluate the different random attempts of a robust scheme allowing to reduce the number of trials in the process. The proposal is tested and evaluated in simulations and with both synthetic and real images.

1. Introduction

In central systems the projection surface of a 3D line is a plane passing through the viewpoint of the camera. In this class of projection some of the information of the 3D line is lost because any 3D line lying on this plane is projected on the same line-image. In other words, a 3D line occludes any other line located behind because the projection surface is a plane.

By contrast, in non-central systems the projection rays do not intersect a common viewpoint. The locus of the viewpoint is, in general, tangent to a caustic (Agrawal et al. (2010)) which is an envelope surface of the projection rays. In particular, when the non-central system is axial and has symmetry of revolution the projection rays intersects the axis of symmetry (see Fig. 1) and the projection surface of a 3D line is composed by skew lines forming a ruled surface. If we consider a set of 4 skew projection rays, being generic lines [1], there exist only two lines intersecting the given set (Teller and Hohmeyer (1999)):the original 3D line and, if the system is axially symmetric, the axis of revolution. This means that no additional line can intersect the set
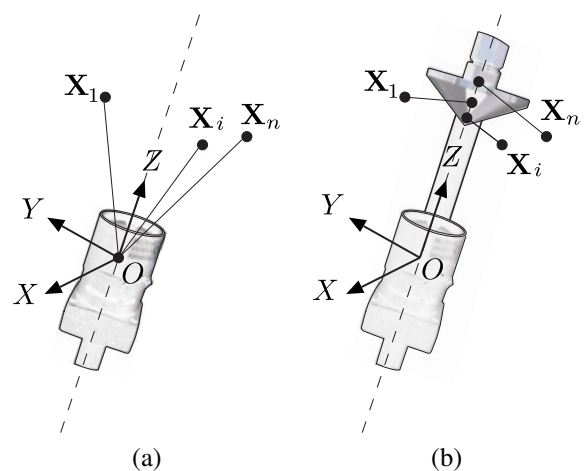
Fig. 1. (a) Central camera: All the projection rays intersect the optical center O. (b) Non-central axial catadioptric camera: Depending on the 3D point X the projection rays intersect a different point of the axis of revolution.

[**]Corresponding author:
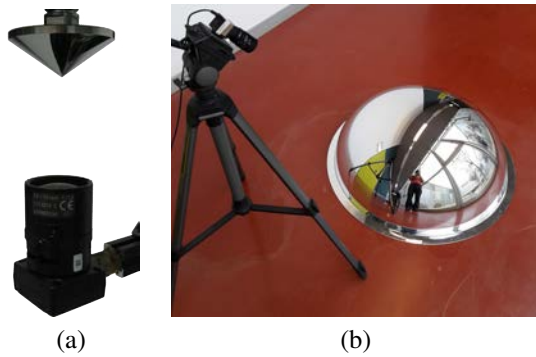 *e-mail:* bermudez@unizar.es (Jesus Bermudez-Cameo)

Fig. 2. (a) Conical catadioptric system. (b) Spherical catadioptric system.

of projection rays. Hence in axial non-central projections, it is not possible to occlude a 3D line with other line. Main consequence of this property is that the complete geometry of a 3D line is mapped on a single non-central image. Therefore, if the system is calibrated, the 3D line can be completely recovered from at least 4 line-image points or projection rays. On the contrary, image-points do not provide 3D information since points always occlude other 3D points along the projection ray.

This property implies a great geometric advantage of lines with respect to points in non-central cameras and generates new possibilities in line-features based 3D vision and entails promising applications in robotics and scene modelling. The richer information about the localization of the line in the space facilitates the tracking of the features even if the photometric information is not very discriminative. Notice also that line features usually represent boundaries of the scene that remain even in texture-less scenes. These advantages have a direct influence in robot pose estimation and Simultaneous Localization and Mapping(SLAM) where texture-less scenes can induce drift in pose estimation due to the lack of significant features.

Some previous approaches have tried to fit 3D lines from a single image in non-central catadioptric systems. The approach presented by Teller and Hohmeyer (1999) exploits the intersection operator between lines for defining a linear system from 4 rays computing the two incident lines. Since in non-central systems with symmetry of revolution one of these lines is the axis of revolution, this approach is used in Caglioti and Gasparini (2005); Caglioti et al. (2007a); Gasparini and Caglioti (2011) for estimating 3D lines from line projections of non-central catadioptric images and studying the degeneracies and singular configurations. In Lanman et al. (2006) the same approach is used with spherical catadioptric mirrors for 3D reconstruction. Work in Swaminathan et al. (2008) extends the approach from lines to planar curves. In Agrawal et al. (2010) the line-image for spherical catadioptric systems is indirectly shown as the epipolar curve. This epipolar curve represents in fact the projection of a 3D line (the epipolar ray of other system) an is represented through a second order line complex. Some simplifications have been used to improve the reconstructions

by reducing the DOFs of the problem: considering horizontal lines (Pinciroli et al. (2005); Chen et al. (2011)), exploiting cross-ratio properties (Perdigoto and Araujo (2012)) or imposing additional constraints such as parallelism or perpendicularity (Bermudez-Cameo et al. (2014a)).

Line projections have been also used to estimate the calibration of non-central systems in a generalization of the plumbline approach. For example in Caglioti et al. (2007b) they exploit that there exists less ambiguity when the system is off-axis with impressive results. However, that approach does not allow to obtain an analytical expression of the line projection. In Agrawal and Ramalingam (2013) they exploit particular geometric properties of spherical mirrors for computing extrinsic calibration parameters. As application, the pose of non-central catadioptric systems is estimated in an image sequence (Miraldo and Araujo (2014); Miraldo et al. (2015)) using known 3D lines.

In Perdigoto and Araujo (2016) a method for estimating the mirror shape and extrinsic parameters for axial non-central catadioptric systems is presented. For the particular case of spherical mirrors quartic curves representing line projections are fitted. For this fitting they propose using the geometric distance by using a generic constrained optimization.

Automatically extracting the projection of a line in non-central images is a challenging task. In omnidirectional central systems the problem differs if the system is calibrated (Puig et al. (2012)) or not. It has been recently solved for calibrated images (Bazin et al. (2010); Ying and Zha (2005)) and for uncalibrated axially symmetric images (Bermudez-Cameo et al. (2015); Tardif et al. (2006)). In non-central images the difficulty of the extraction increases due to the high distortions induced on line-images, the elevated number of degrees of freedom involved in the extraction and the lack of effective baseline of current non-central systems. This problem has been successfully addressed for non-central circular panoramas in Bermudez-Cameo et al. (2017).

In this paper, we study the robust fitting of line projections in non-central catadioptric cameras with symmetry of revolution and present a method for automatic extraction of these line projections. Up to our knowledge, this is the first work addressing this problem in non-central catadioptric cameras. The proposal has been developed for conical catadioptric and spherical catadioptric systems. This procedure automatically segments the collection of edges corresponding to line-images. The complete 3D localization of a line is also recovered from the extraction in a single image even if the accuracy of the result is sensitive to noise. The contributions of this work are the following:

- A unified framework for describing line-images in non-central systems with revolution symmetry.

- Polynomial expressions of the line-images for conical and spherical catadioptric systems.

- A closed-form solution for computing the geometry of the mirror from 5 points lying on a line-image in conical catadioptric systems.

- Solutions based on polynomial roots for computing the

---

[1]Four lines are generic if no two of them are coplanar, no three of them are coconical or cocylindrical, and the four are not cohyperbolic, i.e. do not lie on the same ruled quadric surface.
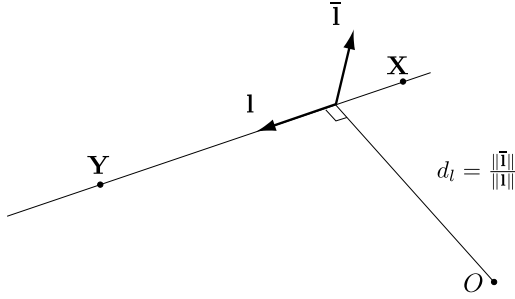
Fig. 3. Euclidean interpretation of Plücker coordinates.

Euclidean distance from point to line-image for conical and spherical catadioptric systems.

- A feature for measuring effective baseline in a set of rays in non-central systems.

- An algorithm for automatic line-image extraction in non-central images.

- Accuracy comparison of line reconstruction between catadioptric systems of similar sizes.

Preliminary results of this work have been presented in Bermudez-Cameo et al. (2014b) where we show the equation of the line-image and the metric distance for conical catadioptric systems. In this paper we extend the approach to spherical catadioptric systems developing the equation of the line-image and the metric distance. We also contribute with the measure of the effective baseline of a set of rays and the automatic line-image extraction procedure. The proposed approaches have been independently validated with a set of simulations. Then the complete pipeline has been tested with synthetic and real images.

In Section 2 we introduce the required background of our proposal. In Section 3 we present our unified framework for describing rays and line projections in non-central systems with symmetry of revolution. In Section 4 we present the proposed description of the line-image for conical catadioptric system and we introduce the computing of the mirror geometry parameter from 5 points of the line-image. In Section 5 we show the polynomial description of the line-image for spherical catadioptric systems and we particularize the corresponding metric distance for this case. In Section 6 we analytically solve the metric distance from a point to the line-image. We particularize the corresponding metric distance for conical and spherical catadioptric systems. In Section 7 we present the algorithm for line-image extraction in non-central images including the proposed feature for measuring the effective baseline of a set of rays. In Section 8 we evaluate the method with synthetic and real images. Finally in Section 9 we present the conclusions.

2. Background

In this section, we introduce the relevant geometric concepts and notation used in this paper. In particular, we summarize the description used for lines, which is based on Grassmann-Cayley algebra (Kanatani (2015)), the transformations between systems of references, and the side operator between two lines.

2.1. Plücker coordinates

The Plücker coordinates of a 3D line (Selig (2004); Pottmann and Wallner (2001)) is an homogeneous representation of a line $\mathbf{L} \in \mathbb{P}^5$ defined by the null space of two $\mathbb{P}^3$ points $\mathbf{X} = (X_1, X_2, X_3, X_4)^\top$ and $\mathbf{Y} = (Y_1, Y_2, Y_3, Y_4)^\top$. When correctly arranged, this representation can be decomposed in two $\mathbb{R}^3$ vectors $\mathbf{L} = \left(\mathbf{l}^\top, \bar{\mathbf{l}}^\top \right)^\top$ defined as

$$\mathbf{l} = X_4 \begin{pmatrix} Y_1 \\ Y_2 \\ Y_3 \end{pmatrix} - Y_4 \begin{pmatrix} X_1 \\ X_2 \\ X_3 \end{pmatrix}, \quad \bar{\mathbf{l}} = \begin{pmatrix} X_1 \\ X_2 \\ X_3 \end{pmatrix} \times \begin{pmatrix} Y_1 \\ Y_2 \\ Y_3 \end{pmatrix}. \quad (1)$$

These vectors have geometrical meaning in Euclidean geometry. $\mathbf{l} \in \mathbb{R}^3$ is called the direction vector and represents the direction of the line. $\bar{\mathbf{l}} \in \mathbb{R}^3$ is called the moment vector and represents the normal to a plane passing through the 3D line and the origin of the reference system O. Not all elements of $\mathbb{P}^5$ correspond to 3D lines. Any point of $\mathbb{P}^5$ corresponding to a line in $\mathbb{P}^5$ must satisfy $\mathbf{l}^\top \bar{\mathbf{l}} = 0$ which is known as Plücker identity. The Euclidean interpretation of this identity is the orthogonality between the direction vector $\mathbf{l}$ and the projection plane vector $\bar{\mathbf{l}}$ (see Fig. 3). The minimum distance from the origin O to the 3D line is computed as $d_l = \frac{\|\bar{\mathbf{l}}\|}{\|\mathbf{l}\|}$.

2.2. Change of reference of Plücker coordinates

Consider $\mathbf{X} \in \mathbb{P}^3$ the representation of a 3D point in homogeneous coordinates in an Euclidean reference system and $\mathbf{X}' \in \mathbb{P}^3$ the representation in another Euclidean reference system; the transformation describing the Euclidean transformation between both reference systems is represented by the matrix

$$\mathsf{T} = \begin{pmatrix} \mathsf{R} & \mathbf{t} \\ \mathbf{0}^\top & 1 \end{pmatrix} \text{ such that } \mathbf{X} = \mathsf{T}\mathbf{X}' \text{ and } \mathbf{X}' = \mathsf{T}^{-1}\mathbf{X}, \quad (2)$$

where $\mathsf{R} \in SO^3$ is a rotation matrix and $\mathbf{t} \in \mathbb{E}^3$ a translation vector. The corresponding transformation for changing the reference of a line $\mathbf{L} \in \mathbb{P}^5$ expressed in Plücker coordinates is

$$\mathsf{G} = \begin{pmatrix} \mathsf{R} & \mathbf{0} \\ [\mathbf{t}]_\times \mathsf{R} & \mathsf{R} \end{pmatrix} : \mathbf{L} = \mathsf{G}\mathbf{L}' \text{ and } \mathbf{L}' = \mathsf{G}^{-1}\mathbf{L}, \quad (3)$$

where $[\mathbf{t}]_\times = \begin{pmatrix} 0 & -t_3 & t_2 \\ t_3 & 0 & -t_1 \\ -t_2 & t_1 & 0 \end{pmatrix}$ is the skew-symmetric matrix operator.

2.3. The side operator

Given two 3D lines expressed in Plücker coordinates $\mathbf{L}_i = \left(\mathbf{l}_i^\top, \bar{\mathbf{l}}_i^\top \right)^\top$ and $\mathbf{L}_j = \left(\mathbf{l}_j^\top, \bar{\mathbf{l}}_j^\top \right)^\top$, the side operator (Pottmann and Wallner (2001)) between them is defined as

$$\mathsf{side}\left(\mathbf{L}_i, \mathbf{L}_j \right) = \mathbf{l}_i^\top \bar{\mathbf{l}}_j + \mathbf{l}_j^\top \bar{\mathbf{l}}_i. \quad (4)$$

The operator $\mathsf{side}\left(\mathbf{L}_i, \mathbf{L}_j \right)$ is a signed distance whose sign defines the side of the line $\mathbf{L}_j$ with respect the line $\mathbf{L}_i$, such that
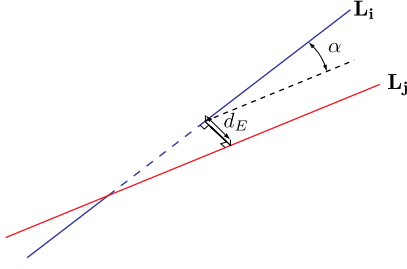
Fig. 4. Distance d_E between two skew rays.

$$|\text{side}\left(\mathbf{L}_i, \mathbf{L}_j\right)| = d_{Eij}\|\mathbf{l}_i\|\|\mathbf{l}_j\| \sin \alpha| \tag{5}$$

where d_{Eij} is the metric distance between the closest point of both lines and α the angle between $\mathbf{l}_i$ and $\mathbf{l}_j$ (see Fig. 4).

3. Line projection in non-central systems

In this section, we present a unified framework for describing rays and line projections in non-central systems with symmetry of revolution.

3.1. Back-projection ray model in non-central systems with revolution symmetry

To exploit the revolution symmetry property we assume that image points $\mathbf{x} = (x, y, z)^\top \in \mathbb{P}^2$ are homogeneous coordinates expressed in a reference centred in the projection of the axis of revolution. This coordinate system is normalized with the camera parameters. The relation between these coordinates and final image coordinates (u, v) is

$$(u, v, 1)^\top \sim \mathsf{K}_c \, \text{distort}\,(\mathsf{R}_{cam}\mathbf{x}) \tag{6}$$

where $\mathsf{K}_c \in \mathbb{R}^3 \times \mathbb{R}^3$ is an affine transformation involving focal length, $\mathsf{R}_{cam} \in SO(3)$ is a rotation matrix and distort is a function introducing a radial distortion model. $\mathbf{x}$ can be expressed in polar coordinates (r, θ, z) such that $r = \sqrt{x^2 + y^2}$ and $\theta = \text{atan2}\,(y, x)$.

In a general non-central system each ray $\Xi\,(\mathbf{x})$ corresponding to an image point is defined by two points (Sturm et al. (2011)), e.g. the 3D point and a point in which the ray is tangent to a surface called caustic. When the system has symmetry of revolution any ray can be expressed in terms of three parameters: elevation angle ϕ, azimuth angle θ and distance from the origin O to the intersection between the ray and the vertical axis Z_r (see Figure 5). We name both the azimuth angle and the polar coordinate presented before as θ because they are equivalent (see Figure 5). The representation of this ray in Plücker coordinates is

$$\Xi = \left(\begin{array}{c} \boldsymbol{\xi} \\ \bar{\boldsymbol{\xi}} \end{array} \right) = \left(\begin{array}{c} \sin \phi \cos \theta \\ \sin \phi \sin \theta \\ \cos \phi \\ -Z_r \sin \phi \sin \theta \\ Z_r \sin \phi \cos \theta \\ 0 \end{array} \right) \tag{7}$$
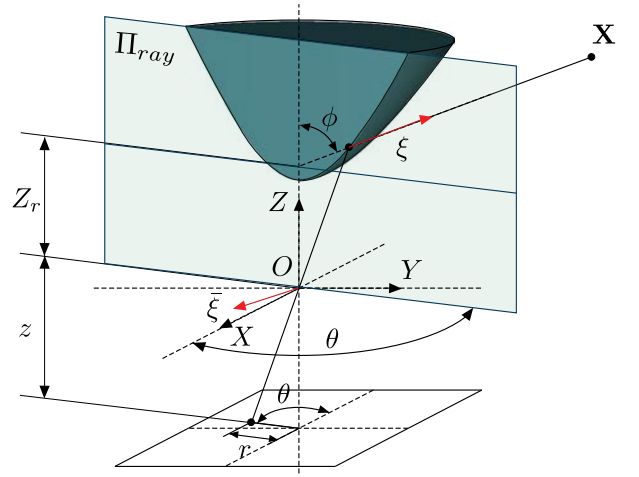

Fig. 5. Back projection of a point (r, θ, z) in non-central catadioptric axial system.

	Conical	Spherical
	$\cot \phi = \frac{z + r \tan 2\tau}{z \tan 2\tau - r}$	$\cot \phi = \frac{-\zeta}{\delta}$
	$Z_r = Z_c + R_c \cot \phi$	$Z_r = Z_s \frac{\delta + \epsilon}{\delta}$

Table 1. Overview of expressions Z_r and $\cot \phi$. Details in Sections 4 and 5.

with $\boldsymbol{\xi} = (\xi_1, \xi_2, \xi_3)^\top$ and $\bar{\boldsymbol{\xi}} = \left(\bar{\xi}_1, \bar{\xi}_2, \bar{\xi}_3\right)^\top$.

The elevation angle $\phi\,(r, z)$ and distance $Z_r\,(r, z)$ have a different expression for computing depending on the kind of system and embed the calibration of the whole system (see Table 1).

3.2. Line projection in non-central systems with revolution symmetry

Consider an image point $\mathbf{x}$. Its corresponding projecting ray $\Xi = \left(\boldsymbol{\xi}^\top, \bar{\boldsymbol{\xi}}^\top\right)^\top$ intersects a 3D line $\mathbf{L} = \left(\mathbf{l}^\top, \bar{\mathbf{l}}^\top\right)^\top$ when

$$\text{side}\,(\Xi, \mathbf{L}) = \boldsymbol{\xi}^\top \bar{\mathbf{l}} + \bar{\boldsymbol{\xi}}^\top \mathbf{l} = 0 \,. \tag{8}$$

Having at least four points and their corresponding rays, the intersection of the projection rays Ξ_i, $i = 1..4$ with the line $\mathbf{L}$ is described by a linear system. In Teller and Hohmeyer (1999) and Gasparini and Caglioti (2011) the solution of this system of equations is used to compute the Plücker representation of the 3D line. Since Plücker coordinates is an over-parametrized representation, the null space of the solution has one dimension. However, not all six-element vectors correspond to a Plücker line. By imposing the Plücker line constraint ($\mathbf{l}^\top\bar{\mathbf{l}} = 0$) two solutions are obtained. One is the axis of symmetry and the other is the sought line.

Notice that there exist some degenerated cases in which projecting surfaces are planes (called Planar Viewing Surfaces (PVS) in Gasparini and Caglioti (2011)) and the geometry of the 3D line cannot be recovered. These degenerated cases are: the Axial-PVS case when the line is coplanar with the axis of symmetry and the Horizontal-PVS case when all the projection rays lie in an horizontal plane ($\phi = \frac{\pi}{2}$).

A line-image is a curve on a two dimensional projected space which defines the collection of rays intersecting a 3D line. This curve is obtained by embedding the back-projection model (7) in equation (8) obtaining

$$Z_r \left(l_2 \cos \theta - l_1 \sin \theta\right) \sin \phi + \left(\bar{l}_1 \cos \theta + \bar{l}_2 \sin \theta\right) \sin \phi + \bar{l}_3 \cos \phi = 0 \,,$$

where l_1, l_2, l_3 are the components of $\mathbf{l}$ and $\bar{l}_1, \bar{l}_2, \bar{l}_3$ are the components of $\bar{\mathbf{l}}$. This equation can be expressed in terms of image coordinates by substituting $\cos \theta = \frac{x}{r}$, $\sin \theta = \frac{y}{r}$ and multiplying by radius r obtaining

$$Z_r \left(l_2 x - l_1 y\right) + \left(\bar{l}_1 x + \bar{l}_2 y\right) + \bar{l}_3 r \cot \phi = 0 \,. \tag{9}$$

which is generalization for non-central systems of the framework proposed in Bermudez-Cameo et al. (2015). With at least 4 points of the line-image we can compute the 3D line in a direct way by solving the linear system

$$(-Z_{ri} y_i, Z_{ri} x_i, x_i, y_i, r_i \cot \phi_i) \, \boldsymbol{\Lambda} = 0 \,, \text{ for } i = 1, ..., 4 \,, \tag{10}$$

where $\boldsymbol{\Lambda} = \left(l_1, l_2, \bar{l}_1, \bar{l}_2, \bar{l}_3\right)^{\mathsf{T}}$. Notice that l_3 has disappeared in the equation and we are obtaining an element of $\mathbb{P}^4$ because the system has revolution symmetry and $\bar{\xi}_3 = 0$. As a consequence, the null space is a single solution instead of the one dimension space obtained when solving (8) in Teller and Hohmeyer (1999). Actually, the Plücker identity used to reduce this space in Teller and Hohmeyer (1999) allows us to compute l_3 due to the redundancy in Plücker coordinates representation.

4. Conical Mirror Systems

In conical catadioptric systems with the camera located in the axis of revolution of the mirror, the locus of viewpoint is a circle of radius R_c centred in the vertical axis at height Z_c (Baker and Nayar (2001); López-Nicolás and Sagués (2014)). The locus of this circle, which depends on the distance Z_m between the camera and the vertex of the mirror, and the aperture angle τ of the mirror, is

$$R_c = Z_m \sin 2\tau \quad , \quad Z_c = Z_m \left(1 - \cos 2\tau\right). \tag{11}$$

4.1. The forward projection model

Since the viewpoint locus is a circle and there exist revolution symmetry the forward projection is unambiguous and direct. Given a 3D point $\mathbf{X} = (X_1, X_2, X_3, X_4)^{\mathsf{T}} \in \mathbb{P}^3$ in the camera reference, the non-central projection ray lies in a plane containing the axis of revolution of the mirror (See Fig. 6). This ray intersects the circle in a point $\mathbf{C}$ placed in the opposite side of the plane (See Fig. 6). The projection ray Ξ is completely defined by $\mathbf{X}$ and $\mathbf{C}$. The reflection of Ξ on the mirror is projected onto point $\mathbf{x} \in \mathbb{P}^2$ on the normalized plane.
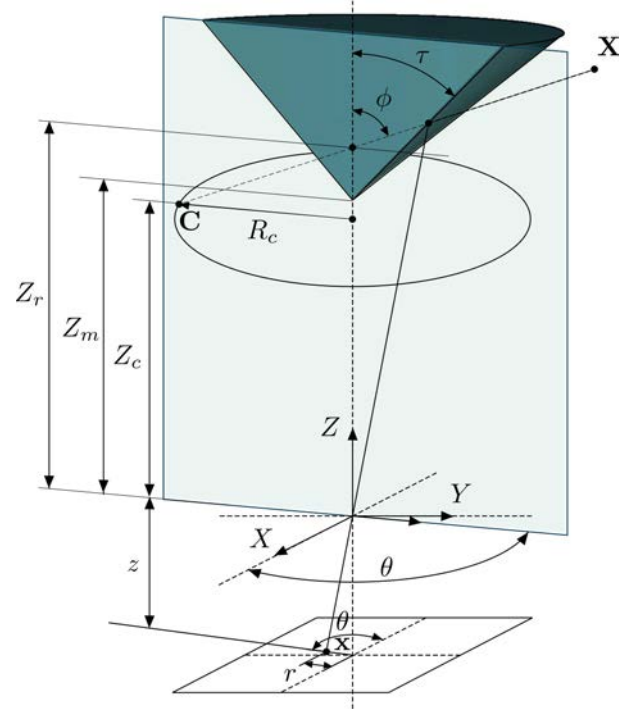

Fig. 6. Conical catadioptric projection of a point X.

$$x = \left(\sin 2\tau \frac{(X_3 - Z_m X_4)}{\sqrt{X_1^2 + X_2^2}} - \cos 2\tau\right) X_1$$

$$y = \left(\sin 2\tau \frac{(X_3 - Z_m X_4)}{\sqrt{X_1^2 + X_2^2}} - \cos 2\tau\right) X_2 \tag{12}$$

$$z = Z_m X_4 + (X_3 - Z_m X_4) \cos 2\tau + \sqrt{X_1^2 + X_2^2} \sin 2\tau$$

This projection is related to the image plane with a perspective camera model involving a linear transformation and a distortion model. We use the projection model of the perspective camera (see (6)) to transform the coordinates of the normalized plane $(x, y, z) \in \mathbb{P}^2$ to the image coordinates $(u, v) \in \mathbb{R}^2$.

4.2. The back projection model

In conical catadioptric systems Z_r depends on $\cot \phi$

$$Z_r = Z_c + R_c \cot \phi \tag{13}$$

which is related with r by

$$\cot \phi = \frac{z + r \tan 2\tau}{z \tan 2\tau - r} \,. \tag{14}$$

Substituting these expressions in (7) the equation of the back projection model becomes

$$\Xi = \begin{pmatrix} x \left(z \tan 2\tau - r\right) \\ y \left(z \tan 2\tau - r\right) \\ r \left(z + r \tan 2\tau\right) \\ -y \left(Z_c \left(z \tan 2\tau - r\right) + R_c \left(z + r \tan 2\tau\right)\right) \\ x \left(Z_c \left(z \tan 2\tau - r\right) + R_c \left(z + r \tan 2\tau\right)\right) \\ 0 \end{pmatrix} . \tag{15}$$

4.3. Line-images in Conical Catadioptric Systems

When particularizing expression (9) to the conical catadioptric system, the line image equation results on a polynomial expression of degree 4 (a quartic described by 15 monomials in general). However, when the equation is expressed in polar coordinates ($x = r \cos \theta$, $y = r \sin \theta$) this expression can be written in a compact form with 6 parameters encapsulating the Plücker coordinates of the line and the mirror parameters of the system. The line-image is then written as

$$(r \cos \theta, r \sin \theta, r, z \cos \theta, z \sin \theta, z)\, \omega = 0 \qquad (16)$$

where

$$\omega = \begin{pmatrix} \omega_1 \\ \omega_2 \\ \omega_3 \\ \omega_4 \\ \omega_5 \\ \omega_6 \end{pmatrix} = \begin{pmatrix} (1 - \cos 2\tau)\, Z_m l_2 - \bar{l}_1 \cos 2\tau \\ -(1 - \cos 2\tau)\, Z_m l_1 - \bar{l}_2 \cos 2\tau \\ \bar{l}_3 \sin 2\tau \\ \sin 2\tau \left(\bar{l}_1 + Z_m l_2 \right) \\ \sin 2\tau \left(\bar{l}_2 - Z_m l_1 \right) \\ \bar{l}_3 \cos 2\tau \end{pmatrix}. \qquad (17)$$

This expression allows us to linearly compute the line-image from five or more points without knowing neither the aperture angle of the mirror τ nor the distance to the mirror Z_m, by solving

$$\left(r_i x_i, r_i y_i, r_i^2, x_i z_i, y_i z_i, r_i z_i \right) \omega = 0 \text{ for } i = 1, ..., 5 . \qquad (18)$$

Once the line-image $\omega \in \mathbb{P}^5$ is estimated τ is computed from $\tan 2\tau = \omega_3/\omega_6$. Notice that the distance to the mirror Z_m is coupled with direction vector $\mathbf{l}$ so it is not possible to separate them. Because of this, we conclude that in conical catadioptric mirrors, if the distance of the camera to the mirror Z_m is unknown, it is not possible to reconstruct the scale of a scene from line-images in a single image.

4.3.1. Parametric Description and Singularity

A parametric description of the line equation can be used for depicting the line projection. Expression (16) allows expressing r in terms of θ

$$r = z \frac{-(\omega_4 \cos \theta + \omega_5 \sin \theta + \omega_6)}{\omega_1 \cos \theta + \omega_2 \sin \theta + \omega_3} \qquad (19)$$

therefore, the parametric expression of the line-image curve becomes

$$x(\theta) = -(\omega_4 \cos \theta + \omega_5 \sin \theta + \omega_6) \cos \theta \qquad (20)$$
$$y(\theta) = -(\omega_4 \cos \theta + \omega_5 \sin \theta + \omega_6) \sin \theta \qquad (21)$$
$$z(\theta) = \omega_1 \cos \theta + \omega_2 \sin \theta + \omega_3 . \qquad (22)$$

In conical catadioptric systems the vertex cone projection ($x = 0$, $y = 0$) is a singularity for line-images passing through it. If the line-image lies on this point, equation (19) returns negative values of r for some values of θ. At the singularity, the curve is continuous but not derivable. Considering the points
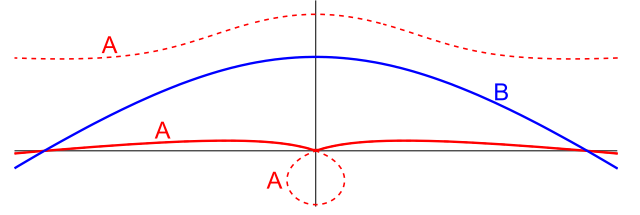

Fig. 7. Detail of two line projections A and B in a non-central catadioptric image with conical mirror. Line A (in red) passes through the singularity at the principal point (dotted points correspond to negative radius).

with negative radius the curve is derivable on the singularity. Actually, these points are not obtained on the real catadioptric image (dotted points in Figure 7).

From equation (19) we can determine the range of values of θ in which the radius is negative. The values of θ limiting this range are computed from

$$\omega_4 \cos \theta + \omega_5 \sin \theta + \omega_6 = 0 , \qquad (23)$$

by substituting $\cos \theta = \frac{1}{\sqrt{1+\tan^2 \theta}}$ and $\sin \theta = \frac{\tan \theta}{\sqrt{1+\tan^2 \theta}}$ in (23) obtaining the following quadratic equation

$$\left(\omega_5^2 - \omega_6^2 \right) \tan^2 \theta + 2\omega_4 \omega_5 \tan \theta + \left(\omega_4^2 - \omega_6^2 \right) = 0 , \qquad (24)$$

with solution

$$\tan \theta = \frac{-\omega_4 \omega_5 \pm \omega_6 \sqrt{\omega_4^2 + \omega_5^2 - \omega_6^2}}{\omega_5^2 - \omega_6^2} . \qquad (25)$$

Notice that it does not exist a real solution if the value inside the square root is negative. In other words, all θ values (19) give $r > 0$ and the line-image does not belong to the singularity. So, we can state that a line-image passes through the singularity if and only if $\omega_4^2 + \omega_5^2 > \omega_6^2$.

5. Spherical Mirror Systems

A spherical catadioptric system is a non-central system composed by a spherical mirror and a perspective camera. Due to the symmetry of the sphere there exist symmetry of revolution wherever the perspective camera is located. The system is characterized by the radius of the sphere R_s, the distance from the camera to the center of the sphere Z_s, the intrinsic parameters of the perspective camera and the relative rotation of the camera with respect to the axis of revolution. This axis is defined by the center of the sphere and the location of the perspective camera.

5.1. The forward projection model

The forward projection in spherical catadioptric systems is tackled in Agrawal and Ramalingam (2013); Agrawal et al. (2011); Gonçalves (2010); Gonçalves and Nogueira (2009). The solution of the forward projection model in this case can be considered as the roots of a polynomial of degree 4. The multiple possible solutions must be tested to identify the one with physical meaning.
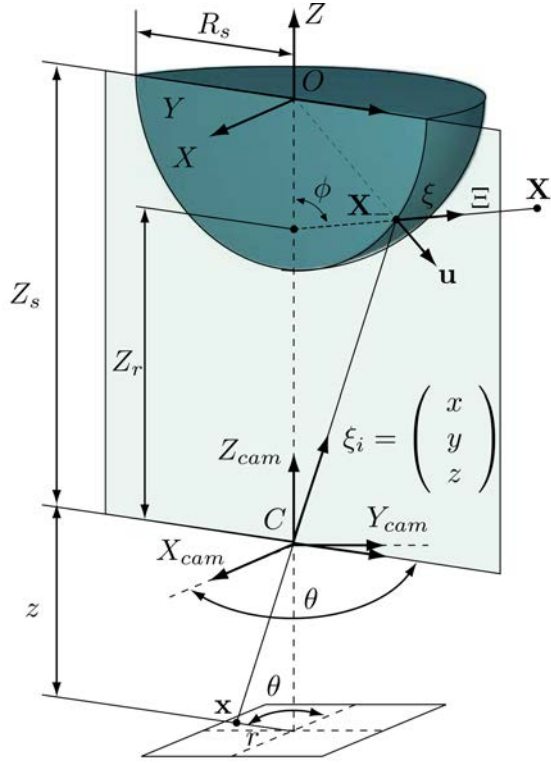
$$\mathbf{U}_T = \mathsf{Q}_s\mathbf{X}_- = \begin{pmatrix} -x\,(Z_{Rel} - 1) \\ -y\,(Z_{Rel} - 1) \\ z + Z_{Rel}\,\sqrt{\gamma} \\ R_s\left(\sqrt{\gamma} + Z_{Rel}z\right) \end{pmatrix}. \quad (28)$$

On the other hand, the Snell's reflection law in Plücker coordinates is defined as

$$\boldsymbol{\xi} = \boldsymbol{\xi}_i\mathbf{u}^\mathsf{T}\mathbf{u} - 2\mathbf{u}\boldsymbol{\xi}_i^\mathsf{T}\mathbf{u} \quad (29)$$
$$\bar{\boldsymbol{\xi}} = 2u_0\boldsymbol{\xi}_i \times \mathbf{u} - \bar{\boldsymbol{\xi}}_i\mathbf{u}^\mathsf{T}\mathbf{u} + 2\mathbf{u}\mathbf{u}^\mathsf{T}\bar{\boldsymbol{\xi}}_i \quad (30)$$

then $\boldsymbol{\Xi} = \left(\boldsymbol{\xi}^\mathsf{T}, \bar{\boldsymbol{\xi}}^\mathsf{T}\right)^\mathsf{T}$ becomes

$$\boldsymbol{\xi} = \begin{pmatrix} x\delta \\ y\delta \\ -\zeta \end{pmatrix}, \quad \bar{\boldsymbol{\xi}} = \epsilon Z_s\begin{pmatrix} -y \\ x \\ 0 \end{pmatrix} \quad (31)$$

with $\delta = 2r^2 Z_{Rel}^4 - 2z\chi Z_{Rel}^2 - 3\rho^2 Z_{Rel}^2 + \rho^2$,

$\epsilon = \left(-r^2 + z^2\right)Z_{Rel}^2 + 2\chi z + \rho^2$ and

$\zeta = 2r^2 z Z_{Rel}^4 - 2\chi\left(-r^2 Z_{Rel}^2 + \rho^2\right) - z\rho^2\left(1 + Z_{Rel}^2\right)$

where $\chi = \sqrt{Z_{Rel}^2\gamma}$.

Notice that $\boldsymbol{\Xi}$ is the back projected ray expressed in the reference of the sphere O. It is transformed to camera reference C through the transformation $\boldsymbol{\Xi}_c = \mathsf{G}_{cs}\boldsymbol{\Xi}$ with

$$\mathsf{G}_{cs} = \begin{pmatrix} 1 & 0 & 0 & 0 & 0 & 0 \\ 0 & 1 & 0 & 0 & 0 & 0 \\ 0 & 0 & 1 & 0 & 0 & 0 \\ 0 & -Z_s & 0 & 1 & 0 & 0 \\ Z_s & 0 & 0 & 0 & 1 & 0 \\ 0 & 0 & 0 & 0 & 0 & 1 \end{pmatrix} \text{ such that} \quad (32)$$

$$\boldsymbol{\Xi}_c = (x, y, -\zeta, -yZ_s\,(\delta + \epsilon), xZ_s\,(\delta + \epsilon), 0)^\mathsf{T} \quad (33)$$

defining the parameters of the model presented in Section 3 $\cot\phi = \frac{-\zeta}{\delta}$ and $Z_r = Z_s\frac{\delta+\epsilon}{\delta}$.

5.3. Line images in Spherical Mirror Systems

Following (8) the side operator between a line $\mathbf{L} = \left(\mathbf{l}^\mathsf{T}, \bar{\mathbf{l}}^\mathsf{T}\right)^\mathsf{T}$ and the projection ray $\boldsymbol{\Xi}$ represented in the sphere reference O defines the line image equation as

$$\epsilon Z_s\,(l_2 x - l_1 y) + \delta\left(\bar{l}_1 x + \bar{l}_2 y\right) - \bar{l}_3\zeta = 0\,. \quad (34)$$

This expression can be developed using the distance Z_s in the description of the line such that $\tilde{\mathbf{l}} = Z_s\mathbf{l}$. Then we can obtain a quartic curve which is rewritten as

$$\hat{\mathbf{L}}^\mathsf{T}\mathsf{N}\hat{\mathbf{X}} = 0 \quad (35)$$

where

Fig. 8. Spherical catadioptric projection of a point X.

5.2. The back projection model

Equation (7) can be particularized to the case of the spherical catadioptric system obtaining the back projection model. The back-projection model in a catadioptric spherical system is obtained by computing the reflection of an incident ray $\boldsymbol{\Xi}_i$ on the sphere following the Snell's law. Consider a reference system placed in O the center of the sphere with radius R_s and described by $\mathbf{X}^\mathsf{T}\mathsf{Q}_s\mathbf{X} = 0$, where $\mathbf{X}$ are 3D points in $\mathbb{P}^3$ and

$$\mathsf{Q}_s = \begin{pmatrix} I_{3\times3} & \mathbf{0} \\ \mathbf{0}^\mathsf{T} & -R_s^2 \end{pmatrix}. \quad (26)$$

Consider also a projective point $\mathbf{x} = (x, y, z)^\mathsf{T}$ in the reference of a perspective camera aligned with the axis of revolution and placed a distance Z_s in $\mathbf{X}_0 = (0, 0, -Z_s, 1)^\mathsf{T}$ and defining an incident ray $\boldsymbol{\Xi}_i$ with direction $\xi_i = (x, y, z)^\mathsf{T}$ equal to $\mathbf{x}$ (see Fig. 8).

The intersection of $\boldsymbol{\Xi}_i$ with the sphere (see Appendix A) gives two points $\mathbf{X}_\pm$ where only $\mathbf{X}_-$ is visible. The expressions of these points are

$$\mathbf{X}_\pm = \begin{pmatrix} -xR_s\,(Z_{Rel} - 1) \\ -yR_s\,(Z_{Rel} - 1) \\ R_s\left(z \mp Z_{Rel}\,\sqrt{\gamma}\right) \\ \pm\sqrt{\gamma} - Z_{Rel}z \end{pmatrix} \quad (27)$$

where $Z_{Rel} = \frac{Z_s}{R_s}$ is the ratio between the distance from the camera and the sphere center and the radius of the sphere, $r^2 = x^2 + y^2$, $\rho^2 = x^2 + y^2 + z^2$ and $\gamma = \left(-r^2 Z_{Rel}^2 + \rho^2\right)$. To compute the reflection we consider the plane $\mathbf{U}_T = \left(\mathbf{u}^\mathsf{T}, u_0\right)^\mathsf{T}$ tangent to the sphere in $\mathbf{X}_-$ such that

$$
\hat{\mathbf{L}} = \begin{pmatrix} \tilde{l}_1^2 \\ \tilde{l}_1 \bar{l}_2 \\ \tilde{l}_1 \bar{l}_1 \\ \tilde{l}_1 \bar{l}_2 \\ \tilde{l}_1 \bar{l}_3 \\ \tilde{l}_2^2 \\ \tilde{l}_2 \bar{l}_1 \\ \tilde{l}_2 \bar{l}_2 \\ \tilde{l}_2 \bar{l}_3 \\ \bar{l}_1^2 \\ \bar{l}_1 \bar{l}_2 \\ \bar{l}_1 \bar{l}_3 \\ \bar{l}_2^2 \\ \bar{l}_2 \bar{l}_3 \\ \bar{l}_3^2 \end{pmatrix}, \qquad \hat{\mathbf{X}} = \begin{pmatrix} x^4 \\ x^3 y \\ x^3 z \\ x^2 y^2 \\ x^2 y z \\ x^2 z^2 \\ x y^3 \\ x y^2 z \\ x y z^2 \\ x z^3 \\ y^4 \\ y^3 z \\ y^2 z^2 \\ y z^3 \\ z^4 \end{pmatrix}
$$

are the lifted coordinates of of the line $\mathbf{L}$ and the image point $\mathbf{x}$ and $\mathsf{N}(Z_{Rel})$ is a 15×15 matrix only depending on Z_{Rel}. The matrix N (see (B.1)) and the 15 coefficients of the quadric $\mathbf{q}_s = \mathsf{N}^\mathsf{T} \hat{\mathbf{L}}$ are detailed in Appendix B.

Notice that this equation does not depend on Z_s (only on the relative measure Z_{Rel}) because we are representing the lifted coordinates $\hat{\mathbf{L}}$ in the sphere reference O and because we have embedded Z_s in $\tilde{\mathbf{I}}$. We can also represent this equation in the reference of the camera by using the transformation $\mathsf{H}(Z_s)$ (see (B.2)) depending on Z_s such that $\hat{\mathbf{L}} = H \hat{\mathbf{L}}_C$ and $\hat{\mathbf{L}}_C^\mathsf{T} \mathsf{H}^\mathsf{T} \mathsf{N} \hat{\mathbf{X}} = 0$.

5.3.1. Parametric Description

The parametric description of the line-image can be obtained composing the lifted image vector $\hat{\mathbf{X}}$ with the polar representation $x = r \cos \theta$, $y = r \sin \theta$ and $z = 1$. When θ is known the result is a polynomial which can be solved for r with the form

$$
\sum_{i=0}^{4} p_i r^i = 0 , \tag{36}
$$

where the coefficients $p_i = f(\mathbf{q}_s, \theta)$ are defined as

$$
p_4 = q_1 \cos^4 \theta + q_{11} \sin^4 \theta + q_4 \cos^2 \theta \sin^2 \theta + ... \tag{37}
$$
$$
... + q_2 \cos^3 \theta \sin \theta + q_7 \cos \theta \sin^3 \theta
$$
$$
p_3 = q_3 \cos^3 \theta + q_{12} \sin^3 \theta + q_5 \cos^2 \theta \sin \theta + q_8 \cos \theta \sin^2 \theta \tag{38}
$$
$$
p_2 = q_6 \cos^2 \theta + q_{13} \sin^2 \theta + q_9 \cos \theta \sin \theta \tag{39}
$$
$$
p_1 = q_{10} \cos \theta + q_{14} \sin \theta \tag{40}
$$
$$
p_0 = q_{15} . \tag{41}
$$

Four different solutions are obtained but only one of them corresponds to the sought parametric line-image. Points corresponding to the right solution must also satisfy equation (35) (see Fig. 9).

6. Algebraic and metric distances

When evaluating if a point belongs to a line-image for fitting the curve is necessary a function measuring the distance from a point to the line-image. The quality of the extracted line-image depends on this distance. In this Section, we present a qualitative comparison among distances and we propose different
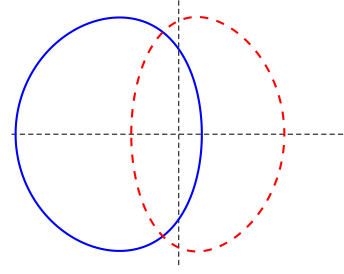

Fig. 9. Representation of the line-image quartic (35) using the parametric description of Section 5.3.1. The whole collection of points satisfies equation (35) but only the points with physical meaning (in continuous blue) satisfy equation (34).

approaches for tackling this problem. Having the line-image equation (9) a measure of distance is the algebraic distance

$$
d_{alg}(\mathbf{x}, L) = |Z_r \left(l_2 \frac{x}{z} - l_1 \frac{y}{z} \right) + \left(\bar{l}_1 \frac{x}{z} + \bar{l}_2 \frac{y}{z} \right) + \bar{l}_3 \frac{r}{z} \cot \phi| \tag{42}
$$

which is measured in pixels when the Plücker coordinates of the line $\mathbf{L}$ are normalized with $\|\bar{\mathbf{l}}\| = 1$.

The second distance considered is the Euclidean metric distance in $\mathbb{E}^3$ which is the minimum Euclidean distance between two 3D lines (the 3D line and the projecting ray generated from an image point). The Euclidean metric distance is defined as in Pottmann and Wallner (2001)

$$
d_E(\mathbf{L}_i, \mathbf{L}_j) = \frac{|\mathbf{l}_i^\mathsf{T} \bar{\mathbf{l}}_j + \mathbf{l}_j^\mathsf{T} \bar{\mathbf{l}}_i|}{\|\mathbf{l}_i \times \mathbf{l}_j\|} \tag{43}
$$

which is defined in 3D space units (meters).

The equidistant region defined by distances d_{alg} and d_E is not homogeneous on the image plane (See Figure 11), particularly in the case of conical catadioptric camera.

Besides, both distances (d_{alg} and d_E) tend to give higher reward to lines closer to the origin, conditioning the robust extraction process. For understanding this effect, in Figure 12 we show the projection of the same horizontal line (conical catadioptric system) but having a different depth. If we set a threshold using a given distance we define a 3D voting region on the space (in red in Figure 12). Consider now that we are trying to robustly fit a line located 1 meter far from our system. If one of the random line hypothesis is very close to the system the region defined by the threshold is so big that any point of any projection is going to vote this hypothesis despite it is not modelling the original 3D line. Another way of posing that is realizing that when using a threshold with a spatial based distance (like d_{alg} or d_E) we define a voting space composed by a set of cylinders which are going to saturate the 3D voting space in a region close to the system, such that any 3D line located in the close region is going to be compatible with the original set of points.

To avoid these effects we propose using the Euclidean distance $\mathbb{E}^2$ from point to line-image on the image plane which is the Euclidean distance between a given point $\mathbf{x} = (x, y, z)^\mathsf{T}$ and the closest point of the line-image $\mathbf{x}_c = (x_c, y_c)^\mathsf{T}$ (see Fig. 10)

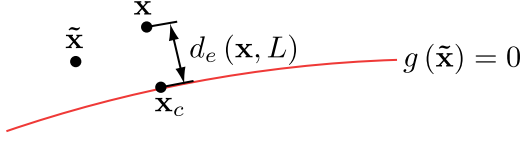**Fig. 10. Euclidean distance from point x to line-image L.**

$$d_e(\mathbf{x}, L) = d_e(\mathbf{x}, \mathbf{x}_c) = \sqrt{\left(\frac{x}{z} - x_c\right)^2 + \left(\frac{y}{z} - y_c\right)^2}. \quad (44)$$

Let $\tilde{\mathbf{x}} = (\tilde{x}, \tilde{y})^\mathsf{T} \in \mathbb{R}^2$ be a point of the image plane. Computing the point of the line-image $\mathbf{x}_c$ which is closer to the given point $\mathbf{x}$ (see Fig. 10), is equivalent to minimizing the distance function $f_d(\tilde{\mathbf{x}}) = d_e(\mathbf{x}, \tilde{\mathbf{x}})$ subject to the constraint $g(\tilde{\mathbf{x}}) = (\tilde{x}, \tilde{y}, 1) = 0$ where g is any representation of the line-image equation (e.g. (9)). Since $\arg\min_{\mathbf{x}} d_e(\mathbf{x}, L) = \arg\min_{\mathbf{x}} d_e^2(\mathbf{x}, L)$ the problem is stated as

$$d_e(\mathbf{x}, L) = d_e(\mathbf{x}, \mathbf{x}_c) \text{ such that } \mathbf{x}_c = \arg\min_{\tilde{\mathbf{x}}} f_d^2(\tilde{\mathbf{x}})$$

$$\text{subject to } g(\tilde{\mathbf{x}}) = 0. \quad (45)$$

The method of Lagrange multipliers justifies that this statement is equivalent to find the critical points of the Lagrangian function

$$\mathcal{L}(\tilde{\mathbf{x}}, \lambda) = f_d^2(\tilde{\mathbf{x}}) + \lambda g(\tilde{\mathbf{x}}), \quad (46)$$

which are estimated by solving $\nabla_{\tilde{x}, \tilde{y}, \lambda} \mathcal{L}(\tilde{x}, \tilde{y}, \lambda) = 0$. Eliminating the Lagrange parameter λ we finally obtain the equation system

$$g(\tilde{\mathbf{x}}) = 0, \quad h(\tilde{\mathbf{x}}) = \left(\tilde{x} - \frac{x}{z}\right)\frac{\partial g}{\partial \tilde{y}} - \left(\tilde{y} - \frac{y}{z}\right)\frac{\partial g}{\partial \tilde{x}} = 0, \quad (47)$$

in such a way that point $\tilde{\mathbf{x}}$ is on the line-image and satisfies that the perpendicular line passing by this point must intersect $\mathbf{x}$. In next sections we solve (47) for the two selected cases of conical and spherical catadioptric systems finding analytical solutions which are roots of a polynomial. This is possible because in these cases the line-image equation g can be written as a polynomial, but in general the solution has to be solved using iterative methods minimizing (47).

6.1. Euclidean distance d_e in conical catadioptric systems

The Euclidean distance $d_e(\mathbf{x}, L)$ between the image point $\mathbf{x}$ and the line-image L is obtained estimating the closest point of the line-image $\mathbf{x}_c$. The point $\tilde{\mathbf{x}} \in \mathbb{E}^2$ of the Euclidean plane is the closest point of the line-image $\mathbf{x}_c$ when satisfying $g(\tilde{\mathbf{x}}) = 0$ and $h(\tilde{\mathbf{x}}) = 0$. Particularizing equation (47) to conical catadioptric systems we can reach a solution based on the roots of a single polynomial equation. Since the degree of the polynomial is greater than four the solution can not be considered a closed-form, however the estimation of the roots of a polynomial is computationally fast and robust.
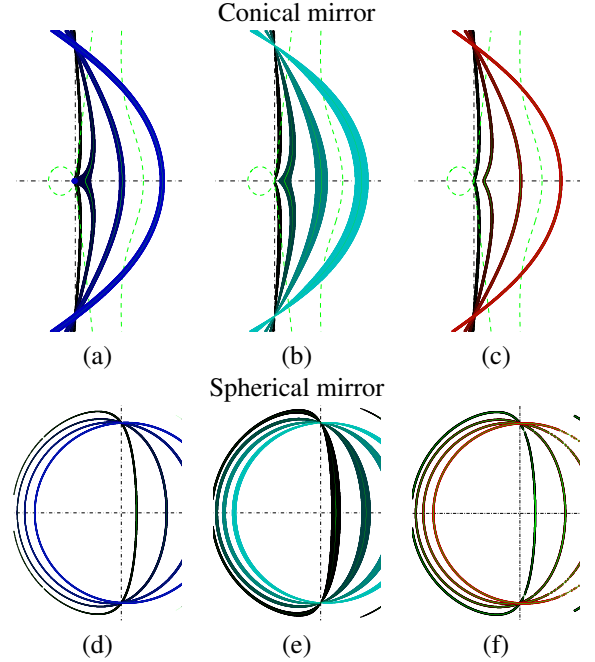

Fig. 11. Comparison of the different metrics presented to decide if a point lies on a line-image. The thin lines are the actual line-images. The coloured region around the lines denotes the points of the region which have a distance minor than a threshold. Example for conical and spherical catadioptric system: (a,d) Algebraic distance d_{alg}, (b,e) Euclidean distance between lines d_E, (c,f) Euclidean distance from point to line-image d_e.
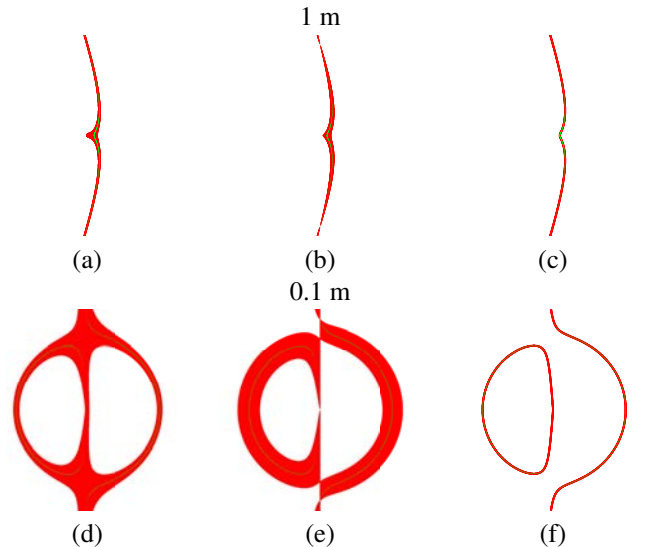

Fig. 12. Region defined by a fixed threshold when using distances d_{Alg}, d_E and d_e in conical catadioptric images. Horizontal line. The size of the regions defined by d_{Alg}, and d_E are strongly dependent on the depth of the line.

First we expand the compact line-image description (16) to get a polynomial equation for $g(\tilde{\mathbf{x}}) = 0$. In this case it yields the quartic

$$g = \tilde{r}^2 (\omega_6 + \omega_1 \tilde{x} + \omega_2 \tilde{y})^2 - (\omega_4 \tilde{x} + \omega_5 \tilde{y} + \omega_3 \tilde{r}^2)^2 = 0 \quad (48)$$

where $\tilde{r}^2 = \tilde{x}^2 + \tilde{y}^2$. The resulting polynomial equation $h(\tilde{\mathbf{x}}) = 0$ obtained from this expression is the quartic

$$\left(\tilde{x}^3, \tilde{x}^2 \tilde{y}, \tilde{x}^2, \tilde{x}\tilde{y}^2, \tilde{x}\tilde{y}, \tilde{x}, \tilde{y}^3, \tilde{y}^2, \tilde{y} \right) \mathsf{W} \begin{pmatrix} \tilde{x} - \frac{x}{z} \\ \tilde{y} - \frac{y}{z} \end{pmatrix} = 0 \quad (49)$$

where

$$\mathsf{W} = \begin{pmatrix} \omega_1 \omega_2 & 2\omega_3^2 - 2\omega_1^2 \\ \omega_1^2 + \omega_2^2 - 2\omega_3^2 & -3\omega_1 \omega_2 \\ \omega_2 \omega_6 - \omega_3 \omega_5 & 3\omega_3 \omega_4 - 3\omega_1 \omega_6 \\ 3\omega_1 \omega_2 & -\omega_1^2 - \omega_2^2 + 2\omega_3^2 \\ 2\omega_1 \omega_6 - 2\omega_3 \omega_4 & 2\omega_3 \omega_5 - 2\omega_2 \omega_6 \\ -\omega_4 \omega_5 & \omega_4^2 - \omega_6^2 \\ 2\omega_2^2 - 2\omega_3^2 & -\omega_1 \omega_2 \\ 3\omega_2 \omega_6 - 3\omega_3 \omega_5 & \omega_3 \omega_4 - \omega_1 \omega_6 \\ \omega_6^2 - \omega_5^2 & \omega_4 \omega_5 \end{pmatrix} \quad (50)$$

Computing the resultant between both equations from variable $\tilde{y}$ we obtain a single polynomial equation depending on $\tilde{x}$ with degree 12.

$$\left(\tilde{x}^{12}, \tilde{x}^{11}, \tilde{x}^{10}, \tilde{x}^9, \tilde{x}^8, \tilde{x}^7, \tilde{x}^6, \tilde{x}^5, \tilde{x}^4, \tilde{x}^3, \tilde{x}^2, \tilde{x}, 1 \right) \Omega \hat{x} = 0 \quad (51)$$

where $\Omega(\omega) \in \mathbb{R}^{13 \times 15}$ (see Appendix C) and $\hat{x} \in \mathbb{R}^{15}$ such that

$$\hat{x} = (x^4, x^3 y, x^3 z, x^2 y^2, x^2 yz, x^2 z^2, \ldots$$
$$xy^3, xy^2 z, xyz^2, xz^3, y^4, y^3 z, y^2 z^2, yz^3, z^4)^\mathsf{T}$$

For a given point on the normalized plane $\mathbf{x} = (x, y, z)^\mathsf{T}$, solving (51) results in 12 solutions for $\tilde{x}$. The correct solution can be found by checking g and h for each solution. From the remaining results we choose the one with minimal distance. Notice that Ω only has to be computed for each line-image ω whereas (51) is solved for each point.

In Fig. 11 we show the different regions defined by the three distances given a threshold. Fig. 11 (a,d) corresponds to the regions for the algebraic distance d_{alg}, observing that there exist variations in the thickness of the region when the projection is close to the center of the image. The region defined by the 3D Euclidean distance between line and rays d_E (see Fig. 11 (b,e)) variates its thickness depending on the distance of the point of the 3D line. Finally, the Euclidean distance on the image d_e defines a region with an homogeneous thickness (see Figure 11 (c,f)).

6.2. Euclidean distance d_e in spherical catadioptric systems

We have shown that the point $\tilde{\mathbf{x}} \in \mathbb{E}^2$ of the Euclidean plane is the closest point of the line-image $\mathbf{x}_c$ when satisfying the systems of equations (47). In particular, when considering a spherical catadioptric system, the function $g(\tilde{\mathbf{x}})$ is defined by the polynomial representation of the line-image (35)

$$g(\tilde{\mathbf{x}}) = \hat{\mathbf{L}}^\mathsf{T} \mathsf{N} \hat{\mathbf{X}}(\tilde{\mathbf{x}}) = 0 . \quad (52)$$

The constraint $h(\tilde{\mathbf{x}})$ enforces the parallelism between the gradient of the line-image and the line passing through the closest point of the line-image and the given point. Substituing the gradients of expression (35) in (47) we obtain

$$h(\tilde{\mathbf{x}}) = \hat{\mathbf{L}}^\mathsf{T} \mathsf{N} \mathsf{J} \hat{\mathbf{X}} = 0 \quad (53)$$

where J is a matrix depending on $\mathbf{x}$ (see (B.3)).

Both expressions $g(\tilde{\mathbf{x}}) = 0$ and $h(\tilde{\mathbf{x}}) = 0$ constitute a polynomial system of equations of degree four. Considering $\tilde{z} = 1$ and the operator

$$\mathrm{tri}(\mathbf{v}) = \begin{pmatrix} 0 & 0 & 0 & 0 & v_1 \\ 0 & 0 & 0 & v_2 & v_3 \\ 0 & 0 & v_4 & v_5 & v_6 \\ 0 & v_7 & v_8 & v_9 & v_{10} \\ v_{11} & v_{12} & v_{13} & v_{14} & v_{15} \end{pmatrix}$$

these equations can be rewritten on terms of a bi-quartic expression.

$$g = \tilde{\mathbf{x}}_Q^\mathsf{T} \mathrm{tri}\left(\hat{\mathbf{L}}^\mathsf{T} \mathsf{N} \right) \tilde{\mathbf{y}}_Q = 0 \quad (54)$$

$$h = \tilde{\mathbf{x}}_Q^\mathsf{T} \mathrm{tri}\left(\hat{\mathbf{L}}^\mathsf{T} \mathsf{N} \mathsf{J} \right) \tilde{\mathbf{y}}_Q = 0 \quad (55)$$

where $\tilde{\mathbf{x}}_Q = \left(\tilde{x}^4, \tilde{x}^3, \tilde{x}^2, \tilde{x}, 1 \right)^\mathsf{T}$ and $\tilde{\mathbf{y}}_Q = \left(\tilde{y}^4, \tilde{y}^3, \tilde{y}^2, \tilde{y}, 1 \right)^\mathsf{T}$.

One of the two variables of the systems of equations can be eliminated computing the resultant between them. For this, we compute the Sylvester matrix S respect to $\tilde{y}$ obtaining a 8×8 matrix. The determinant of this matrix is the resultant, that is a polynomial equation such that

$$|S| = 0 \Leftrightarrow g = 0 \text{ and } h = 0. \quad (56)$$

To reduce the difficulty of computing this determinant we exploit the property of determinants

$$|S| = \begin{vmatrix} S_A & S_B \\ S_C & S_D \end{vmatrix} = |S_A| \left| S_D - S_C S_A^{-1} S_B \right| .$$

where $S_A = S_{1..4,1..4}$, $S_B = S_{1..4,5..8}$, $S_C = S_{5..8,1..4}$ and $S_D = S_{5..8,5..8}$. Since $|S_A| \neq 0$ the degree of the resultant decreases, obtaining the determinant of a 4×4 matrix

$$|S_L| = \left| S_D - S_C S_A^{-1} S_B \right| = \left| \sum_{k=1}^{8} \sum_{m=1}^{3} \bar{\mathsf{S}}_{km} \tilde{x}^{k-1} x_m \right| = 0 \quad (57)$$

with $x_m = \{x_1 = x, x_2 = y, x_3 = z\}$ and $\bar{\mathsf{S}}_{km} \in \mathbb{R}^{4 \times 4}$ such that

$$\bar{\mathsf{S}}_{km} = \begin{pmatrix} \bar{s}_{11km} & \bar{s}_{12km} & \bar{s}_{13km} & \bar{s}_{14km} \\ \bar{s}_{21km} & \bar{s}_{22km} & \bar{s}_{23km} & \bar{s}_{24km} \\ \bar{s}_{31km} & \bar{s}_{32km} & \bar{s}_{33km} & \bar{s}_{34km} \\ \bar{s}_{41km} & \bar{s}_{42km} & \bar{s}_{43km} & \bar{s}_{44km} \end{pmatrix} \quad (58)$$
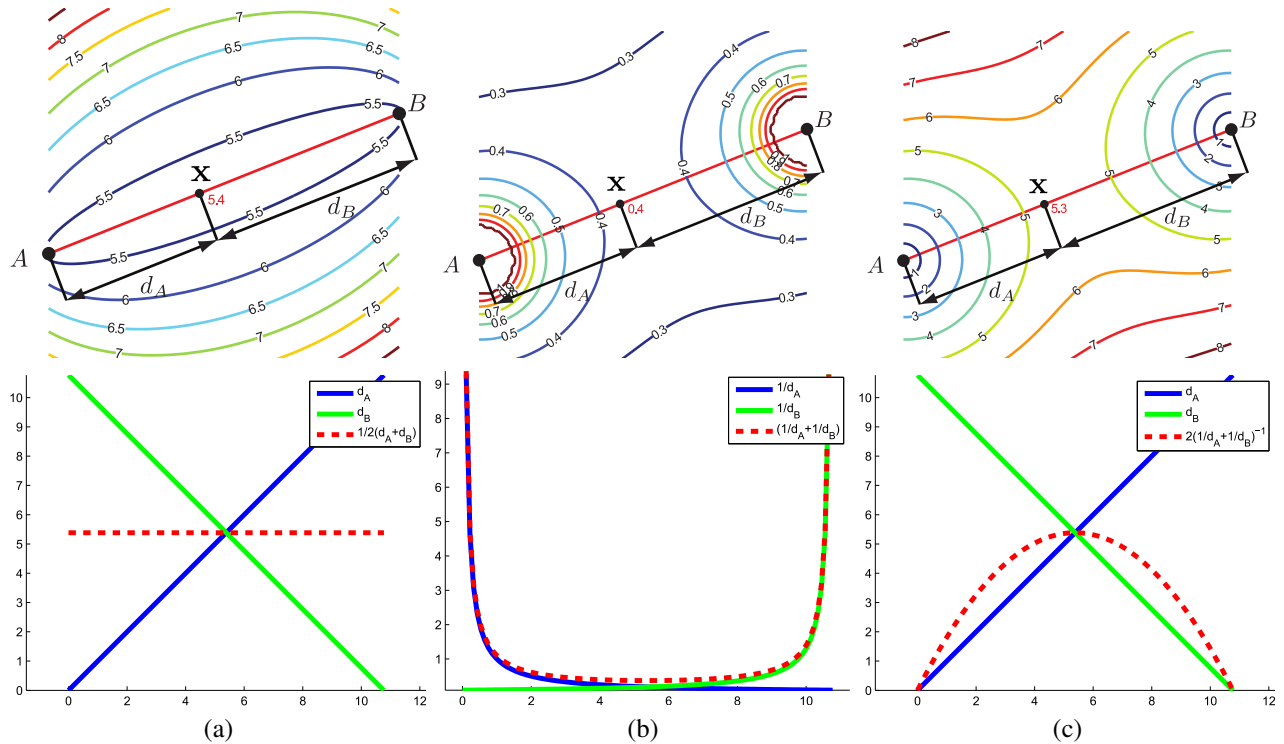
Fig. 13. Different proposals for computing a measure of baseline of a set of rays based on the distances between rays. Consider a point x located d_A from a point A and a distance d_b from a point B. Top: Contour lines of the measure. Bottom: Section of the field of measures along the straight line passing through A and B.(a) Mean of the distances: In this case any point located in the red straight line passing through A and B is going to have the same mean value. However points located close to A or B are bad conditioned because one of the two distances is low. (b) Sum of inverse of the distances: In this case the measure increases rapidly when one of the distances is close to zero. (c) Inverse of the sum of inverse of distances: The maximum of this measure is located in the point equidistant to both reference points A and B.

where $\bar{s}_{ijkm} = f\left(\hat{\mathbf{L}}, \mathsf{N}, \mathsf{J}\right)$ (see Appendix D for more details). When expanding this determinant we obtain a polynomial of degree 16 in $\tilde{x}$

$$|S_L| = \sum_{n=0}^{16} c_n \tilde{x}^n = 0 , \qquad (59)$$

where $c_n = f\left(\bar{s}_{ijkm}, \mathbf{x}\right)$ (see Appendix D for more details).

The roots of this polynomial are the solutions of $\tilde{x}$ for the equation system. Using (54) we obtain 4 solutions of $\tilde{y}$ for each of the 16 solutions obtained for $\tilde{x}$. Each pair $\tilde{\mathbf{x}}_i = (\tilde{x}_i, \tilde{y}_i)^\mathsf{T}$ corresponds to a candidate to be the closer point from the line-image to the original point $\mathbf{x}$. The correct solutions must hold (54) and (34). From the remaining solutions we choose the one with minimal Euclidean distance d_e.

7. Robust line extraction in non-central systems

In this Section, we present a method for line-image extraction in non-central systems. Line extraction in non-central systems is an unsolved challenging task due to the difficulties of mapping the 3D of the line on a 2D space, the sensitivity to noise in fitting, and the elevate number of degrees of freedom involved. Up to our knowledge, this is the first work addressing this problem.

Assuming the system is calibrated, four points of the line-image are needed to define a line-image and its corresponding 3D line. When using a robust approach like RANSAC the number of iterations is considerably greater than in the central case because the number of DOFs increases from 2 to 4. To handle this problem we can check the candidates for minimal subsets before computing the minimal model like in PROSAC (Chum and Matas (2005)) and USAC (Raguram et al. (2013)). That allows to reduce the number of hypotheses being computed and evaluated. In particular, we remove collections of four samples having low effective baseline. The baseline of a set of four points is estimated using our proposal for measuring the effective baseline presented in the following Section. To evaluate if an image point belongs to a particular line-image hypothesis we use the Euclidean distance d_e presented in Section 6.

7.1. A feature for measuring effective baseline in a set of rays

To compute a 3D line from a set of rays (see Section 3.2) the rays must not be coplanar. Consider for example a set of four rays intersecting a line, two of them being projections in a camera and the other two projections in other camera of a stereo pair. If we get a ray from a camera and a ray from the other camera they are skew and there exist a distance between them related with the baseline of the stereo system. The accuracy of the line reconstruction is strongly related with this distance. Similarly, when having a non-central system, the accuracy of the reconstruction of a 3D line from a single projection strongly depends on the distances between the defining rays which depend on the geometry and the size of the imaging system. In

this section we propose a feature measuring the quality of a set of rays for reconstructing a 3D line. Establishing a similarity with the stereo pair we call this measure *effective baseline*.

The proposed feature is based on the 3D Euclidean distances among the defining rays d_{Eij} (43). Consider the combination of distances among a set of defining rays; a simple feature is just the mean among all these distances. However, the mean distance is not a good choice. For example we can have a high mean distance due to a sole distant ray but if the other rays are coplanar the configuration is degenerated.

To measure the effective baseline of a set of n rays our proposal is the function z_{bs} depending on the Euclidean distances $d_E\left(\Xi_i, \Xi_j\right)$ among the defining rays

$$z_{bs} = \frac{n!}{2\,(n-2)!} \left(\sum_{i=1}^{n-1} \sum_{j=i+1}^{n} \frac{1}{d_E\left(\Xi_i, \Xi_j\right)} \right)^{-1} \qquad (60)$$

which takes into account the balance among the distances. This function increases when the distances between rays increase but also assures that not any individual distance $d_E\left(\Xi_i, \Xi_j\right)$ turns to zero. The feature is normalized with the number of combinations $\frac{n!}{2(n-2)!}$ in order to have a scaled measure.

To illustrate our reasoning let us first consider a simple case (see Fig 13). Let us consider two points A and B in $\mathbb{R}^2$ and we want to evaluate a third point **x** using the distances from this third point to the other two (d_A and d_B). The higher the distances the better the result, but we need to penalize small individual distances.

If we use the mean of the distances we have infinite cases and some of these cases with values of d_A or d_B close to zero (see Fig 13 (a)) which are degenerated cases. However, inspired by electrical potentials, we could use the sum of the inverse of the distance defining a potential surface which is the minimum at the equidistant point (see Fig 13 (b)) which is the best conditioned case. However, this measure tends to infinity when one of the distances is zero, hence considering the inverse of this (see Fig 13 (c)) we have a feature which is maximum when the distances are balanced.

7.2. Extraction algorithm

The proposed extraction procedure is the following. First, the image is preprocessed using a Rolling Guidance Filter (Zhang et al. (2014)) to reduce textured patterns but conserving the edges. Then, the edges of the image are detected using Canny detector and stored in connected components. Each of these connected components can contain one or more line-images. A particular line-image can also be distributed along different connected components. We have considered two different robust strategies for solving the multi-fitting process required to extract line-images from the edges.

Greedy PROSAC approach. In this approach we check the candidates for minimal subsets using the effective-baseline measure. From the subsets that achieve this previous test we compute the line-image models. Then, all the points of the connected component are tested using the corresponding metric distance. In robust approaches like RANSAC it is assumed that the input of the algorithm is a collection of points fitting a single model. The points not supporting the model are discriminated as outliers. When having more than one model or line-image, the greedy approach considers a cascade application of the robust estimation. The model best supporting the collection of points is extracted. For the other models there are two options: First repeating the complete extraction on the remaining points until reaching some stop criterion. Second, removing the inlier points from the original votes matrix of the first extraction and use these corrected votes for selecting new lines. Second way is faster because hypothesises and distances are computed only once.

Greedy approach selecting a subset of well conditioned points. In this approach we compute a subset of well conditioned points from each connected component. The subset of points is big enough to homogeneously cover the whole connected component and it is computed using the effective baseline measure to assure that there exist enough baseline among any collection of four points from this subset. Hypotheses are generated from this subset of points and then tested using the metric distance. The distance can be computed from each hypothesis to the whole collection of points of the connected component or from the subset of points only. In this case, the supporting points are computed only on the best voted solution. Another option is testing the hypothesis with points of the whole image. The greedy cascade approach is used for the multi-fitting process using any of the previously presented methods.

8. Experimental evaluation

In this section, we present the experimental evaluation of the proposal. First, we show simulations to study the behaviour of the proposed method. Then we present selected examples of line-extraction in synthetic and real images. Experiments with synthetic images allow testing the complete algorithm knowing the ground truth and with absence of calibration errors. The extraction method is also tested in images taken with real catadioptric systems. Finally we present several examples of calibration estimation in conical catadioptric systems using real images.

8.1. Validation of the proposals using simulated projections

For validating the proposals we have performed intensive simulations of line projections where the ground truth is known and randomly generated, the noise and calibration error are controlled and it is possible to obtain results with stochastic meaning. The general set-up of the simulation is the following: We consider random segments of 10 m length passing through a cube 4 meters wide around the visual system. For each segment, points are projected on the image using the forward projection model. The size of all the simulated systems is similar to avoid the bias in effective baseline. The conical mirror has an angle $\tau = 45\ deg$ and the distance from the perspective camera to the mirror is $Z_m = 1\ m$. The spherical mirror has a radius of $R_s = 1\ m$ and the distance from the perspective camera to the center of the sphere is $Z_s = 2\ m$ (the distance to the mirror plus
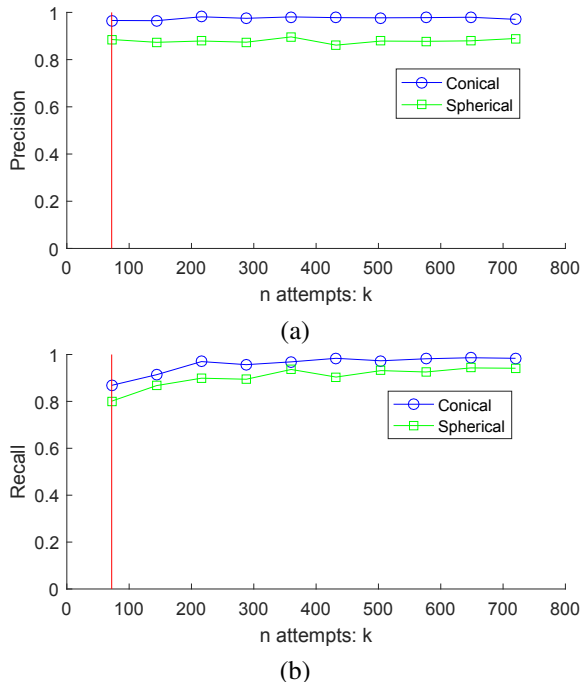
Fig. 14. Precision and recall when discriminating between two line-images.

the radius). The size of the perspective camera used in both systems is 4096×4096 pixel with a focal distance of 2560 pix and neither radial nor tangential distortion.

8.1.1. Robustness evaluation of line-image extraction

In this section, we evaluate the robustness of the extraction process. This is performed by discriminating between two different line-images. 64 pairs of random segments with the previous set-up are projected. Points supporting the first line-image are considered inliers and points supporting the other are considered spurious. We extract the line-image variating the number of attempts k in the RANSAC scheme taking as reference the theoretical value $k = \frac{\log(1-P)}{\log(1-\eta^p)}$ where p is the number of elements defining the minimal set, P the probability that at least in one random subset p all selected points are inliers and $\eta = \frac{number\ of\ inliers}{total\ number\ of\ points}$.

In Fig. 14 we show the results of precision and recall depending on the number of attempts k in robust extraction, where

$$precision = \frac{true\ positives}{true\ positives + false\ positives}$$

and

$$recall = \frac{true\ positives}{true\ positives + false\ negatives}.$$

In line-extraction high precision is needed because a single false positive can distort the fitting. To evaluate the quality of the extraction we propose using the metric distance from point to line-image. In particular, we measure the median of the distances from the fitted line-image to the ground truth points projected from the original line.

8.1.2. Accuracy of 3D line from single view

In this section, we present an evaluation of the 3D accuracy of the extracted lines from a single projection. We show the ob-

tained accuracy when using the classical linear fitting approach (Teller and Hohmeyer (1999)) and the refined accuracy using the Euclidean proposed distance presented in Section 6 as residual. We also compare, in terms of 3D line accuracy, the conical catadioptric system and the spherical catadioptric system. With the described set-up 300 line segments are projected on the image. Then, we add Gaussian noise to points forming the line-images with standard deviation σ from 0 to 1 pixel. Finally, the lines are fitted using all the projected points (100 points).

In boxplot of Fig. 15 (a-b) we present the estimated accuracy showing the distribution of two errors:

- The direction error between the estimated 3D line and the ground truth computed as
  $\epsilon_\phi = \arccos\left(\mathbf{l}^\mathsf{T}\mathbf{l}_{GT}\right)$.

- The depth error between the estimated 3D line and the ground truth computed as $\epsilon_d = \left|\|\bar{\mathbf{l}}\| - \|\bar{\mathbf{l}}_{GT}\|\right|$.

In general, we can consider that the conical catadioptric system responds better than the spherical one, in terms of accuracy in direction and distance estimation despite they have similar sizes. Our intuition for this behaviour is that the round surface of the spherical mirror provokes a softer transition in the rays definition of the projection surfaces that at the end provokes a lower distance between rays. Consider the case of depth estimation (Figure 14 (b)) when using a spherical catadioptric systems; we notice that, with image errors greater than $\sigma > 1$ pixels, it is not possible to properly perform a 3D reconstruction and we observe a saturation in the distance error ϵ_d. We interpret that with high noise the ambiguity of the curve has increased enough to obscure the depth information. With respect to the accuracy of the estimations obtained with the optimization using the d_e distance, we can observe in general an increase of accuracy with respect to the linear estimation. However in most cases, this improvement is not enough to overcome the ambiguity resulted by the noise effect. An exception of that is the case of direction estimation in conical catadioptric systems where the accuracy is considerably improved even when having $\sigma > 2$ pixels.

To evaluate the accuracy of the fitting in terms of the line-image fitting we also present the error in the coefficients defining the quartic curve of the line-image. Since the coefficients of the polynomial are arranged in a 15 dimensional homogeneous vector $\mathbf{q} \in \mathbb{R}^{15}$ (see $\mathbf{q}_c$ for the conical case and $\mathbf{q}_s$ for the spherical case in Appendix B) we have defined the following error $\epsilon_q = \arccos\left(\frac{1}{\|\mathbf{q}\|\|\mathbf{q}_{GT}\|}\mathbf{q}^\mathsf{T}\mathbf{q}_{GT}\right)$ which represents the angular deviation of the $\mathbb{R}^{15}$ normalized vector (see Fig. 15 (c)).

Finally, we have also evaluated what is the behaviour of a line-image when introducing a Gaussian noise in the polynomial coefficients. In Figure 17 we can see the representation of 25 different randomized variations of the normalized vector $\mathbf{q}$ containing the coefficients of the polynomial which describes a given line-image. We have considered errors with a standard deviation of $\sigma = 0.01, 0.001, 0.001$.

8.1.3. Evaluation of effective baseline in line fitting

In this section we evaluate the relation between effective baseline (60) and the accuracy in line fitting. The calibration
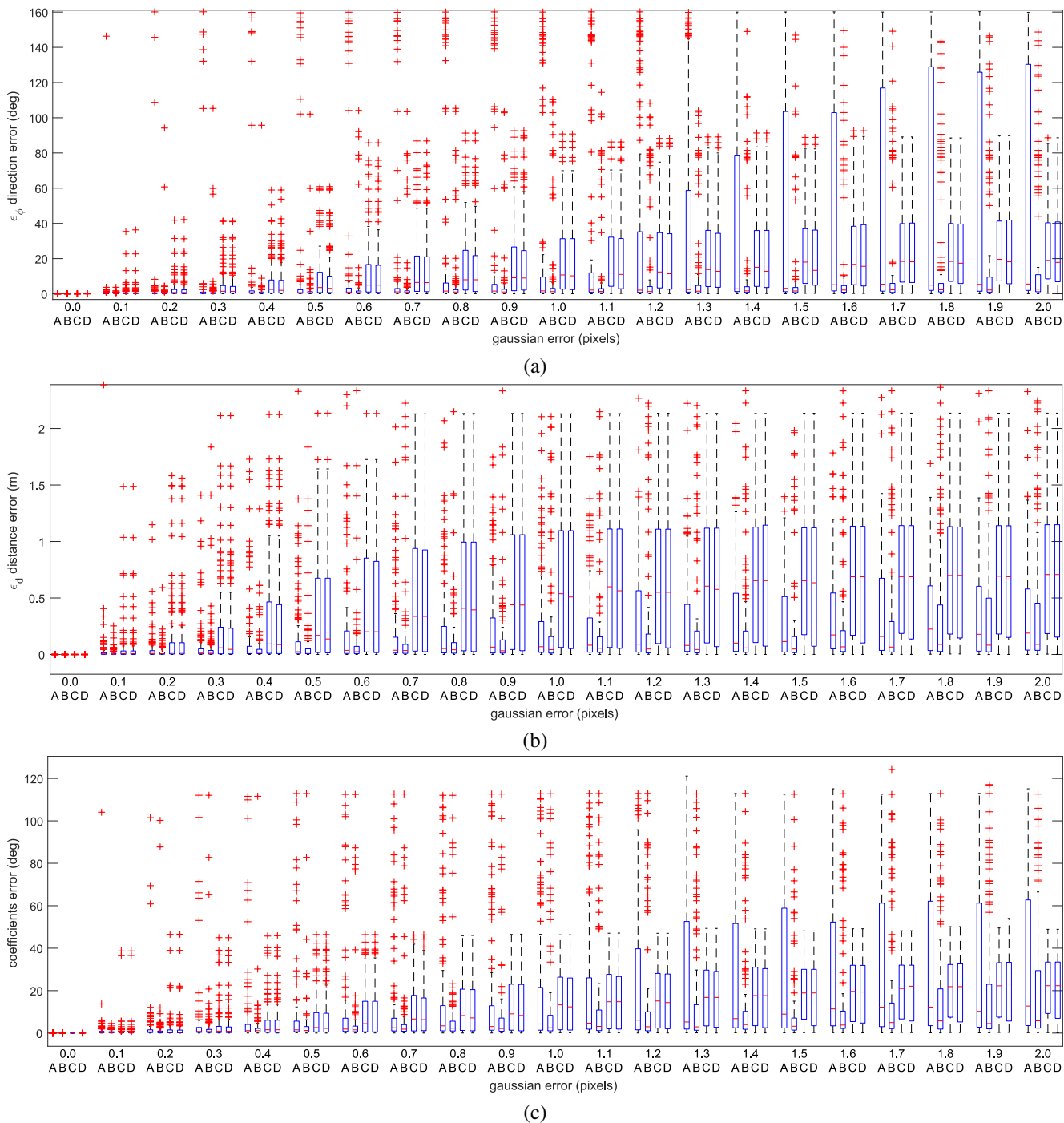
Fig. 15. Comparison of accuracy of linear fitting and optimization fitting for conical and spherical catadioptric systems. (a) Direction error in degrees ϵ_ϕ. (b) Distance error in meters ϵ_d. (c) Coefficients errors in degrees ϵ_q. A stands for linear fitting in conical catadioptric systems; B stands for optimized fitting in conical catadioptric systems; C stands for linear fitting in spherical catadioptric systems and D for optimized fitting in spherical catadioptric systems.
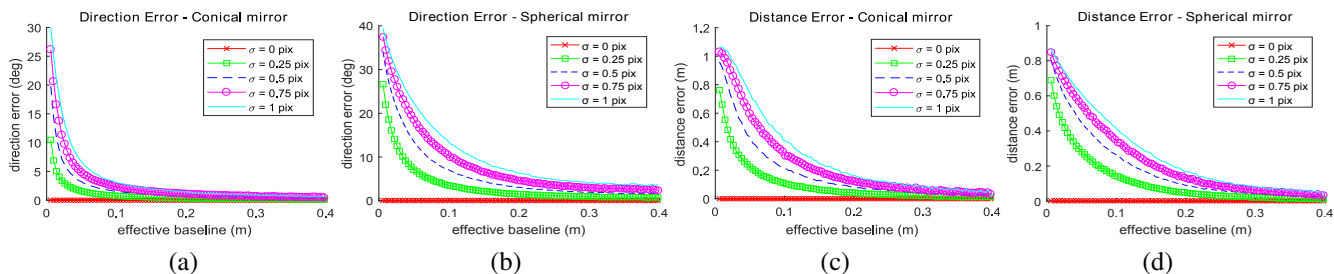
Fig. 16. Evaluation of line fitting accuracy with respect to the effective baseline between the 4-set points lying on the line-image.

Conical Mirror

$\sigma = 0.0001$ $\sigma = 0.001$ $\sigma = 0.001$

Spherical Mirror

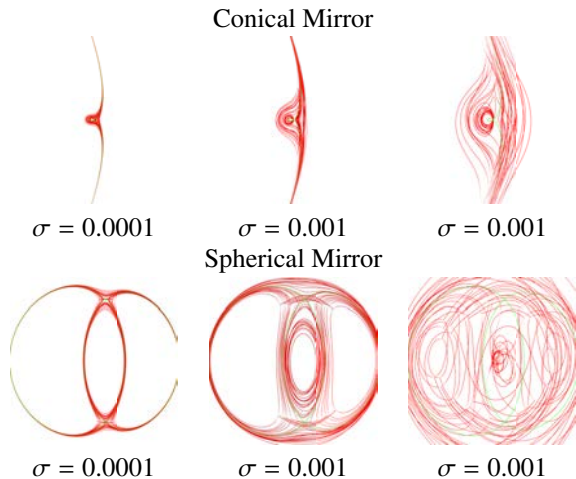$\sigma = 0.0001$ $\sigma = 0.001$ $\sigma = 0.001$

Fig. 17. Variations in parametric representation of line-images when considering Gaussian noise in the polynomial coefficients.

set-up is a conical catadioptric mirror with $\tau = 65$ *degs* and $Z_m = 1m$ and a spherical mirror with $R_S = 1\ m$ and $Z_s = 2\ m$. From a set of 1000 random segments, we define 1000 combinations of 4 points lying on each line-image. Notice that each combination of 4 points has an associated effective baseline. In Fig. 16 we show the accuracy of line fitting with respect the effective baseline of the given set of four points. For that we have quantized the effective baseline of all the sets of four points and computed the error in line fitting. The vertical axis corresponds to the median of the error (direction error for (a,b) and distance error for (c,d)) and the horizontal axis to the corresponding effective baseline. We can observe how the error decreases with a bigger effective baseline in different cases with different amounts of Gaussian noise.

8.1.4. Evaluation of the Euclidean distance d_e definition

In this section, we present a comparison in terms of computational time between (A) the estimation of the Euclidean distance by obtaining the roots of the proposed polynomial (Sections 6.1 and 6.2) and (B) the constrained general formulation (45) as in Perdigoto and Araujo (2016). We have focused on the spherical case comparing our approach with the initial solution and the constraints proposed in Perdigoto and Araujo (2016). In the Perdigoto's approach the initialization is obtained as follows:

- First, the intersection of the line passing through the Origin and the quartic is computed. Notice that this polynomial solution is the same as in presented in Section 5.3.1 for the parametric representation just by computing the angle θ of the given point.

- Then, this initial solution is used in a constrained optimization which corresponds with equation (45) directly. We have implemented it using the fmincon function in Matlab.

- As in our proposal, once we have estimated the closed point to the curve we compute the L2 norm to it.

| | Desktop computer | | | | Laptop | | | |
| | Polynomial | | General | | Polynomial | | General | |
n_p	med.	std	med.	std	med.	std	med.	std
100	0.52	0.01	7.82	1.52	1.11	0.03	13.38	0.03
250	0.50	0.01	7.92	0.94	1.06	0.03	13.49	0.03
500	0.49	0.01	7.91	0.83	1.04	0.03	13.47	0.03
750	0.49	0.01	7.90	0.83	1.04	0.03	13.51	0.03
1000	0.48	0.01	7.89	0.77	1.04	0.03	13.53	0.03

Table 2. Time invested (milliseconds) in computing the distance of a point to a quartic.

For evaluation the comparison we have generated a set of randomized points along the image and we have computed the Euclidean distance d_e from each point to the projection of the previous simulations 300 randomized lines. In Table 2 we can see the median and the standard deviation of the computational time per point using both approaches. For measuring the scalability of both approaches we present results from $n_p = 100$ to 1000 points. The experiment has been run in a desktop computer (Intel Core-i7 6700 3.4 Ghz) and in a Laptop computer (Intel Core i7-2630M 2.00 Ghz). We can see how, in terms of computational time the polynomial approach is considerably more efficient (ten times).

8.2. Line-image extraction

In this section, we present the experiments for evaluating the complete extraction algorithm in synthetic and real images.
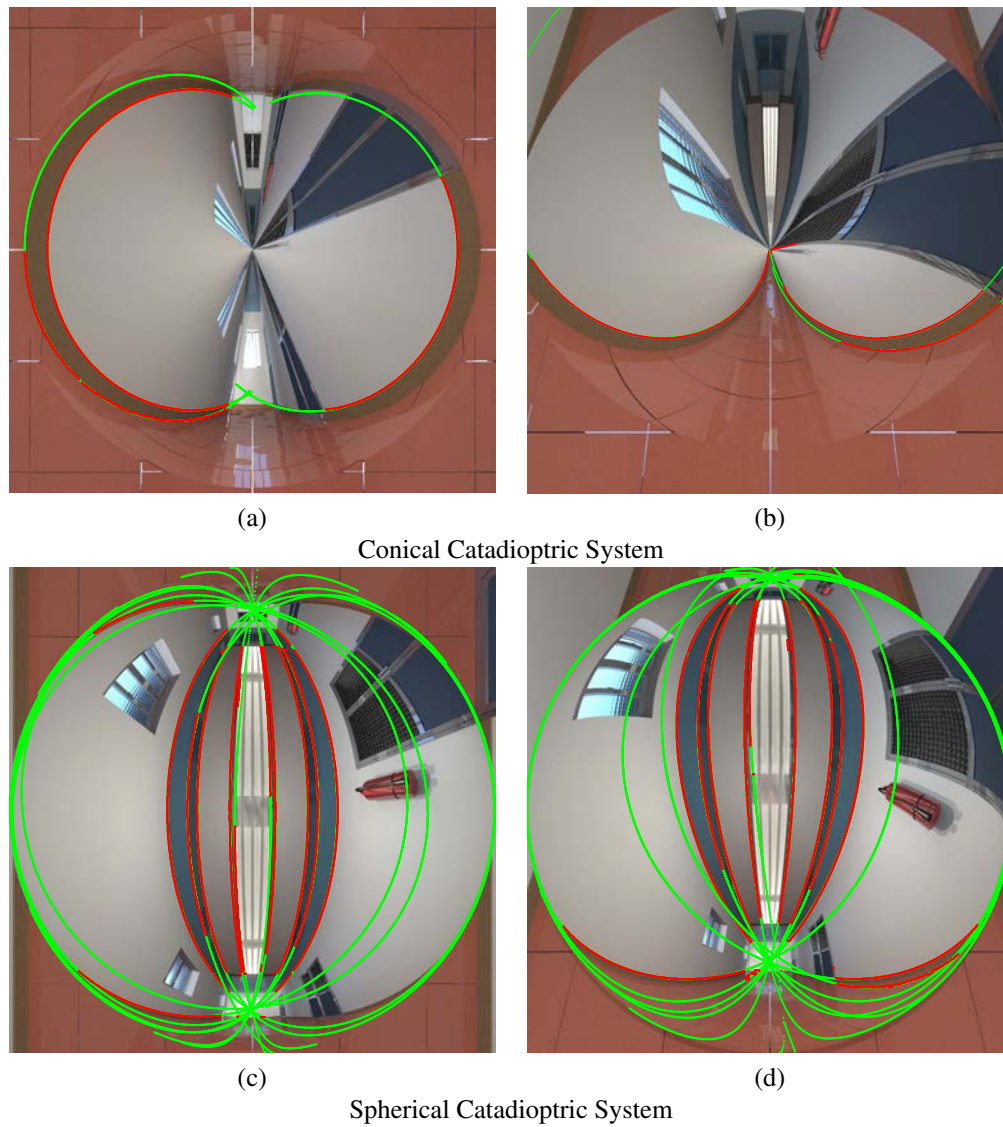
8.2.1. Synthetic images

Synthetic images have been generated using the raytracing software Pov-Ray [2] modelling the mirrors as geometric forms with perfect reflection. The scenario is a modification of a publicly available synthetic scenario [3]. The original office has been modified to look like a corridor. The synthetic images have a size of 1024×1024 pixels. The conical mirror has a radius $R_{max} = 30\ mm$ and height $h_{max} = 21.01\ mm$, i.e. of $\tau = 55\ deg$. The distance from the mirror to the camera is $Z_m = 1\ m$. The spherical mirror has a radius of $R_s = 1.25\ m$ and the distance between the center of the sphere and the camera is $Z_s = 2m$. In Fig. 18 we show some examples of extracted lines from synthetic catadioptric images. The extracted line-images are shown in green and the supporting points in red.
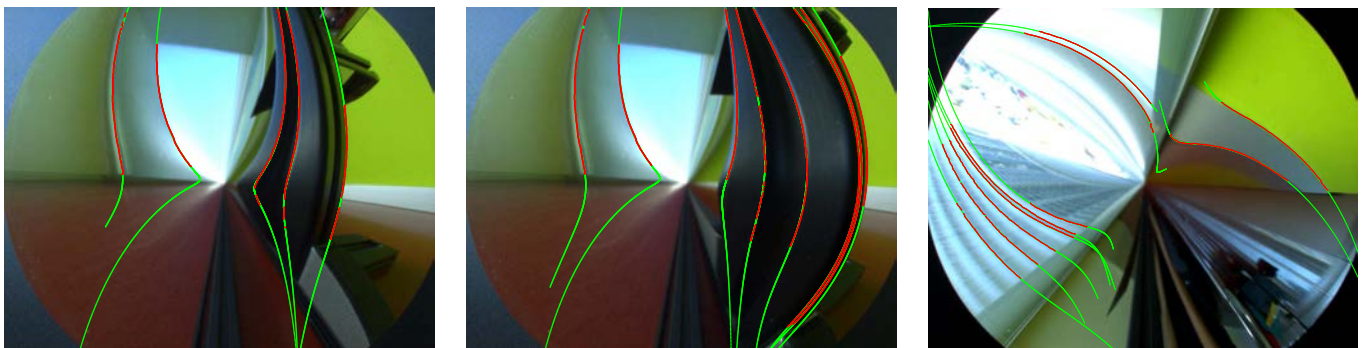
8.2.2. Real Images

The real images have been acquired using two catadioptric systems composed by a conventional camera (uEye UI-148xSE-C) and two mirrors, one conic and other spherical. The conventional camera has a size of 1280×1024 pixels and has been independently calibrated using a standard method. Parameters taken into account are focal distance, principal point, skew and radial distortion. The conical mirror has an aperture angle of $\tau = 55\ deg$ and the system has been manually fixed to

---

[2] http://www.povray.org

[3] http://hof.povray.org/office-13.html The Office - Jaime Vives Piqueres, 2004

(a)   (b)

Conical Catadioptric System

(c)   (d)

Spherical Catadioptric System

Fig. 18. Line-extraction examples from synthetic images. A selection of line-images correctly extracted are shown. The extracted line-images are shown in green and the supporting points in red. (a-b) Conical catadioptric system. (c-d) Spherical catadioptric system.

Fig. 19. Line-extraction examples from real images with conical catadioptric system. A selection of line-images correctly extracted are shown. The extracted line-images are shown in green and the supporting points in red.
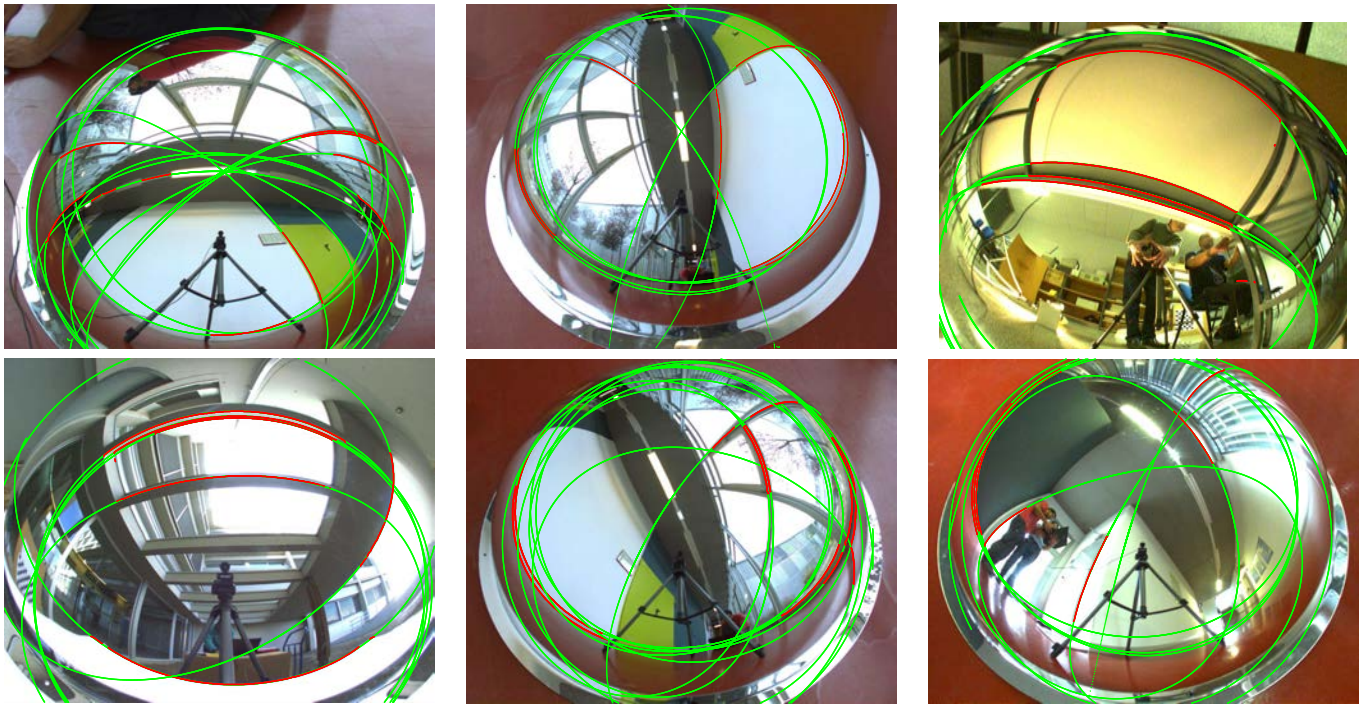
Fig. 20. Line-extraction examples from real images with spherical catadioptric system. A selection of line-images correctly extracted are shown. The extracted line-images are shown in green and the supporting points in red.

assure the alignment between the camera and the mirror with symmetry of revolution. The spherical mirror has a radius of $R_s = 0.37\ m$. Since a spherical catadioptric system is always axial we do not need to enforce the alignment between camera and mirror but we need to calibrate the rotation of the camera with respect to the axis of revolution. The calibration of the system parameters Z_{Rel} and the rotation matrix is estimated by minimizing the forward projection error of a chess pattern of known dimensions.

In Fig. 19 and Fig. 20 we show some examples of the line-image extraction for different real non-central catadioptric images. The extracted line-images are shown in green and the supporting points in red. Just to illustrate the 3D performance of these extractions we show a planarity measure of lines defining planar structures. We have manually chosen the extracted lines defining the table in Fig. 20 top-right. We compute the mean plane defined by these lines. The mean angular deviation of the direction of lines with respect this plane is 3.08 deg (mean of absolute value of error) and standard deviation 2.72 deg. In the case of segments defining the open ceiling in the outdoor scene (Fig. 20 bottom-left) the effective baseline is lower because of the higher distance of lines, obtaining worse results (14.5 deg in mean with standard deviation of 21.96 deg).

8.3. Estimation of geometry of the conical mirror

In this section, we show some examples of fitting using five points manually selected and we present quantitative results in the estimation of the mirror geometry from lines in real images. Five points from conical catadioptric images (in red) are selected manually to compute the line-image ω, which is painted on the image using the parametric description (22). From each
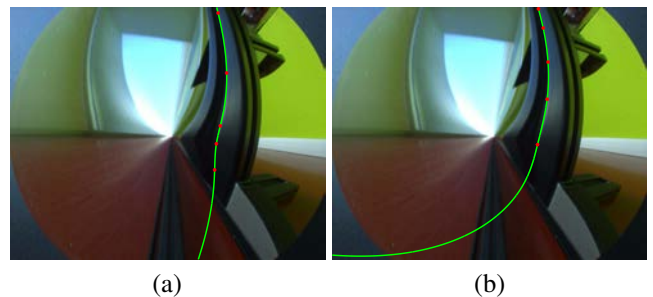

(a)　　　　　　　(b)

Fig. 21. Influence of points selection. (a) Good fitting (b) Bad fitting. We can see the high influence of detected points in line extraction.

line-image ω we extract the Plücker coordinates of the line and the aperture angle of the mirror τ. As explained in Section 4.3, the distance to the mirror Z_m is coupled with the Plücker coordinates. Therefore, the metric in recovered 3D lines is scaled to this distance.

In Figure 21 we show the high influence of error and point selection. Depending on the selected points the line-image fits or not the projected points of the line. Despite both line-images are fitting the defining points and the rest of the projected point of the segment, the error in the estimation of the 4 DOFs complicates the correct extraction of the line. In Figure 22 we show some examples of line projections correctly fitted in different images and the obtained value for τ in each one. We can see how this value is close to the ground truth which is $\tau_{ref} = 55\ deg$. Finally, in Figure 23 we show more examples of incorrect fittings, due to the sensitivity of line projection and the large number of degrees of freedom of the curve in non-central systems.
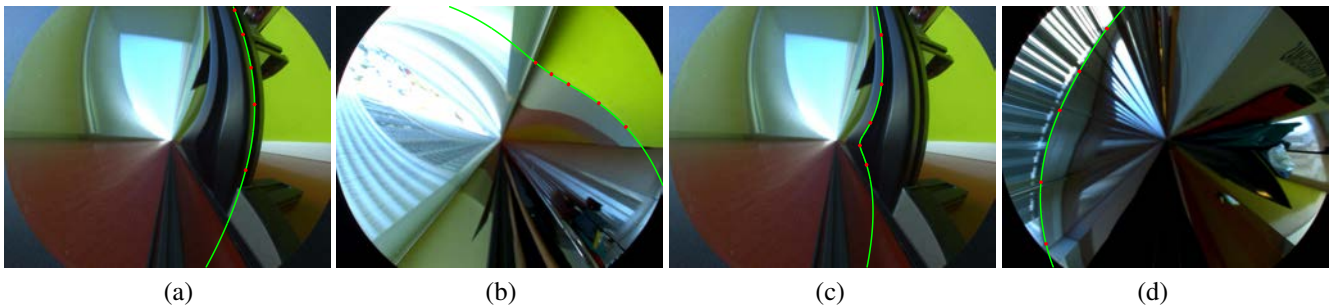
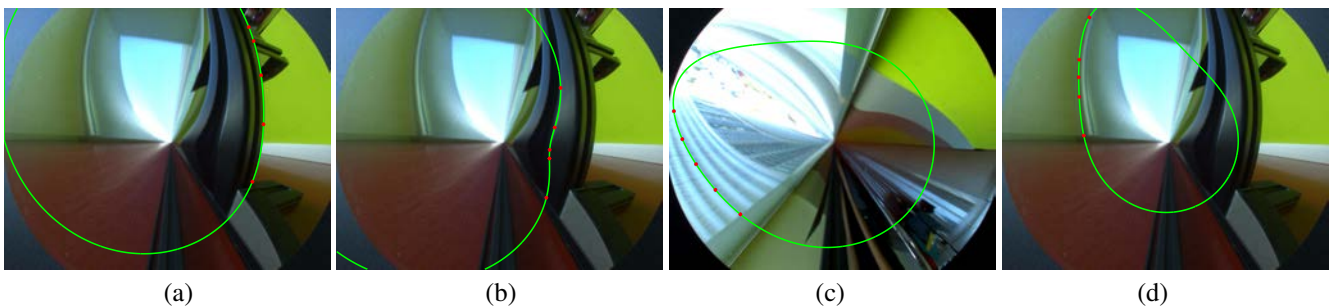**Fig. 22. Examples of correct fitting. (a)** $\tau = 55.0\ deg$**. (b)** $\tau = 55.5\ deg$**. (c)** $\tau = 56.1\ deg$**. (d)** $\tau = 54.9\ deg$**.**

Fig. 23. Examples of incorrect fitting. (a) $\tau = 50.9\ deg$**. (b)** $\tau = 51.1\ deg$**. (c)** $\tau = 49.7\ deg$**. (d)** $\tau = 48.4\ deg$**.**

9. Conclusions

In this paper, we have analyzed the geometry of line projections in non-central catadioptric systems focusing on conical and spherical catadioptric cameras. In both cases line-images are quartic polynomials, although in the conical case it can be simplified to a compact description of 6 homogeneous parameters. The underlying structure of line-images has been used for designing a line-image extraction method and to obtain the geometry of the mirror in the case of the conical catadioptric camera. In non-central cameras, it is possible to recover the complete geometry of the original projected line from a single projection. In this context, our proposal has promising applications in robotics (e.g., robot pose estimation and SLAM) and scene modeling (e.g., 3D reconstruction). Next step in line-image extraction is including energy based approaches to improve the labelling of supporting points by discrete optimization (Isack and Boykov (2012)). However, from the results it follows that despite the line-image extraction can be correctly achieved, the lack of effective baseline of non-central catadioptric systems encourage to investigate new types of non-central cameras allowing accurate 3D reconstructions from single projections. Another feasible approach is exploiting the redundancy along a sequence of images for improving the 3D reconstruction accuracy. As future work we also consider studying the uncertainty propagation of features in order to integrate the extraction scheme in SLAM algorithm.
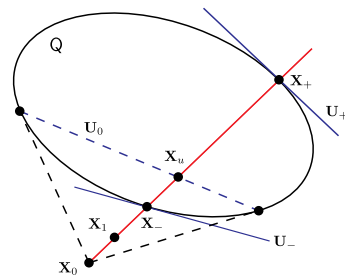
Acknowledgements

Fig. A.24. Section of a quadric. In red a 3D line intersecting the quadric. In Blue, the tangent planes $U_\pm$ and the polar plane U_0.

Appendix A. Intersection of a line with a Quadric

To compute the intersection of a line with a quadric we can follow analogous reasoning to the used in the intersection of a line with a conic on the image (Barreto (2003)).

Consider a central camera located in point $\mathbf{X}_0$ and a point in a projection plane $\mathbf{X}_1$ the Plücker matrix for the line $\mathcal{L}$ is computed by $\mathcal{L} = \mathbf{X}_0\mathbf{X}_1^\mathsf{T} - \mathbf{X}_1\mathbf{X}_0^\mathsf{T}$. This Plücker matrix $\mathcal{L}$ has 6 different components corresponding to the Plücker coordinates of the ray $L = \left(\mathbf{l}, \bar{\mathbf{l}}\right)^\mathsf{T}$.

$$\mathcal{L} = \begin{pmatrix} -\left[\bar{\mathbf{l}}\right]_\times & -\mathbf{l} \\ \mathbf{l}^\mathsf{T} & 0 \end{pmatrix} \tag{A.1}$$

The points of the projecting ray can be expressed in terms of two points of the line with a parameter λ.

$$\mathbf{X}\left(\lambda\right) = \mathbf{X}_1 + \lambda\mathbf{X}_0 \tag{A.2}$$

Consider also the quadric defined by the homogeneous matrix $\mathsf{Q} \in \mathbb{R}^4 \times \mathbb{R}^4$, $\mathsf{Q} = \mathsf{Q}^\mathsf{T}$ (Hartley and Zisserman (2000)) such

that the points lying on the quadric satisfy the homogeneous equation $\mathbf{X}^\mathsf{T}\mathbf{Q}\mathbf{X} = 0$. The plane $\mathbf{U}_0 = \mathbf{Q}\mathbf{X}_0$ is the plane polar to the quadric $\mathbf{Q}$ respect to the pole $\mathbf{X}_0$ which is a plane intersecting the quadric such that any tangent plane to the quadric passing through a point of this intersection contains the pole $\mathbf{X}_0$. Finally, consider the point $\mathbf{X}_u$ which is the intersection between the line with the polar plane $\mathbf{U}_0$ (see Fig. A.24). It is called the conjugate point of $\mathbf{X}_0$ and it can be computed as

$$\mathbf{X}_u = \mathcal{L}\mathbf{U}_0 = \mathcal{L}\mathbf{Q}\mathbf{X}_0 \tag{A.3}$$

Then we can express the line in terms of $\mathbf{X}_0$ and $\mathbf{X}_u$.

$$\mathbf{X}(\lambda) = \mathbf{X}_u + \lambda\mathbf{X}_0 \tag{A.4}$$

The ray intersects the quadric in two points $\mathbf{X}_+$ and $\mathbf{X}_-$. These are two different real points if the ray intersects the quadric, one double point if the ray is tangent to the quadric and two complex points if not (complex in terms of complex numbers). Consider the polar plane $\mathbf{U}$ of a generic point $\mathbf{X}(\lambda)$ of the line

$$\mathbf{U} = \mathbf{Q}\mathbf{X}(\lambda) = \mathbf{Q}\mathbf{X}_u + \lambda\mathbf{Q}\mathbf{X}_0 \tag{A.5}$$

If the point $\mathbf{X}(\lambda)$ is in the quadric its corresponding polar plane $\mathbf{U}$ is tangent to the quadric and passing through the pole. Imposing the point $\mathbf{X}(\lambda)$ lying on plane $\mathbf{U}$ we can solve the intersection.

$$\mathbf{X}^\mathsf{T}\mathbf{U} = \mathbf{X}_u{}^\mathsf{T}\mathbf{Q}\mathbf{X}_u + \lambda\left(\mathbf{X}_u{}^\mathsf{T}\mathbf{Q}\mathbf{X}_0 + \mathbf{X}_0{}^\mathsf{T}\mathbf{Q}\mathbf{X}_u\right) + \lambda^2\mathbf{X}_0{}^\mathsf{T}\mathbf{Q}\mathbf{X}_0 = 0 \tag{A.6}$$

Since $\mathbf{X}_0$ and $\mathbf{X}_u$ are conjugate points $\mathbf{X}_u{}^\mathsf{T}\mathbf{Q}\mathbf{X}_0 = 0$ and $\mathbf{X}_0{}^\mathsf{T}\mathbf{Q}\mathbf{X}_u = 0$ and the last equation remains

$$\mathbf{X}^\mathsf{T}\mathbf{U} = \mathbf{X}_u{}^\mathsf{T}\mathbf{Q}\mathbf{X}_u + \lambda^2\mathbf{X}_0{}^\mathsf{T}\mathbf{Q}\mathbf{X}_0 = 0 \tag{A.7}$$

From these we obtain the parameter λ and the corresponding expressions of the intersections and of the polar planes in these points (which are tangent to the quadric).

$$\lambda^2 = -\frac{\mathbf{X}_u{}^\mathsf{T}\mathbf{Q}\mathbf{X}_u}{\mathbf{X}_0{}^\mathsf{T}\mathbf{Q}\mathbf{X}_0} = -\frac{\mathbf{X}_0{}^\mathsf{T}\mathbf{Q}\mathcal{L}^\mathsf{T}\mathbf{Q}\mathcal{L}\mathbf{Q}\mathbf{X}_0}{\mathbf{X}_0{}^\mathsf{T}\mathbf{Q}\mathbf{X}_0} \tag{A.8}$$

$$\mathbf{X}_\pm = (\mathcal{L}\mathbf{Q} + \lambda I)\mathbf{X}_0, \quad \mathbf{U}_\pm = (\mathbf{Q}\mathcal{L} + \lambda I)\mathbf{Q}\mathbf{X}_0 \tag{A.9}$$

Appendix B. Matrix and polynomial definitions

This appendix presents in Fig. B.25 the matrix expressions which are referred to in Section 5. It also includes the coefficients defining the polynomial representation of the line-image such that $\mathbf{q}_c{}^\mathsf{T}\hat{\mathbf{X}} = 0$ for the case of conical catadioptric system and $\mathbf{q}_c{}^\mathsf{T}\hat{\mathbf{X}} = 0$ for the case of spherical catadioptric system. The coefficients are,

$$\mathbf{q}_c = \begin{pmatrix} \omega_1^2 - \omega_3^2 \\ 2\omega_1\omega_2 \\ 2\omega_1\omega_6 - 2\omega_3\omega_4 \\ \omega_1^2 + \omega_2^2 - 2\omega_3^2 \\ 2\omega_2\omega_6 - 2\omega_3\omega_5 \\ \omega_6^2 - \omega_4^2 \\ 2\omega_1\omega_2 \\ 2\omega_1\omega_6 - 2\omega_3\omega_4 \\ -2\omega_4\omega_5 \\ 0 \\ \omega_2^2 - \omega_3^2 \\ 2\omega_2\omega_6 - 2\omega_3\omega_5 \\ \omega_6^2 - \omega_5^2 \\ 0 \\ 0 \end{pmatrix} \quad \mathbf{q}_s = \begin{pmatrix} s_3^2 + s_1^2 \\ -2s_2s_1 \\ 2s_6s_4 \\ 2s_3^2 + s_2^2 + s_1^2 \\ 2s_6s_5 \\ s_7^2 - s_9^2 \\ -2s_2s_1 \\ 2s_6s_4 \\ s_{10}^2 \\ 2s_6s_7 \\ s_2^2 + s_3^2 \\ 2s_6s_5 \\ s_8^2 - s_{11}^2 \\ -2s_6s_8 \\ s_6^2 \end{pmatrix} \tag{B.4}$$

where

$$s_1 = Z_s l_2 - \bar{l}_1 \nu \tag{B.5}$$
$$s_2 = Z_s l_1 + \bar{l}_2 \nu \tag{B.6}$$
$$s_3^2 = \bar{l}_3^2\left(\nu^2 - 1\right) \tag{B.7}$$
$$s_4 = \bar{l}_1 - Z_s l_2 \nu \tag{B.8}$$
$$s_5 = \bar{l}_2 + Z_s l_1 \nu \tag{B.9}$$
$$s_6 = \bar{l}_3 \tag{B.10}$$
$$s_7 = Z_s l_2 + \bar{l}_1 \tag{B.11}$$
$$s_8 = Z_s l_1 - \bar{l}_2 \tag{B.12}$$
$$s_9^2 = \bar{l}_1^2 + (2\nu + 1)\left(\bar{l}_1^2 + \bar{l}_3^2\right) \tag{B.13}$$
$$s_{10}^2 = 2\left(Z_s l_2 \bar{l}_2 - Z_s l_1 \bar{l}_1 - Z_s l_1 l_2 - \bar{l}_1 \bar{l}_2 (2\nu + 1)\right) \tag{B.14}$$
$$s_{11}^2 = \bar{l}_2^2 + (2\nu + 1)\left(\bar{l}_2^2 + \bar{l}_3^2\right) \tag{B.15}$$

with $\nu = 2Z_{Rel}^2 - 1$.

Appendix C. Omega description

The expressions of the coefficients of matrix Ω are too big to be presented in a written form. We include this definition as the Matlab function `getOmega.m` in the supplementary material [4].

Appendix D. Spherical resultant computation

Consider the quartic coefficients based representation $\mathbf{g} = \mathbf{q}_s = \mathbf{N}^\mathsf{T}\hat{\mathbf{L}}$ such that $g = \mathbf{g}^\mathsf{T}\hat{\mathbf{X}} = 0$ (see (52)). Also, consider the quartic coefficients based representation $\mathbf{h}(\mathbf{x}) = \begin{bmatrix} \mathbf{h}_x, \mathbf{h}_y, \mathbf{h}_z \end{bmatrix}\mathbf{x} = \mathbf{J}^\mathsf{T}\mathbf{N}^\mathsf{T}\hat{\mathbf{L}}$ with $\mathbf{h}, \mathbf{h}_x, \mathbf{h}_y, \mathbf{h}_z \in \mathbb{R}^{15}$ such that $h = \mathbf{h}^\mathsf{T}\hat{\mathbf{X}} = 0$ (see (53). The coefficients $\bar{s}_{ijkm} = f\left(\mathbf{h}_x, \mathbf{h}_y, \mathbf{h}_z, \mathbf{g}\right)$ of the matrix $\bar{S}$ are defined in the Matlab function `getSBar.m` in supplementary material. The coefficients c_n depending on $\bar{s}_{ijkm}$ are defined in the Matlab function `getCoeffsForSolving4x4Det.m` in the supplementary material [4].

[4] http://webdiis.unizar.es/%7Ebermudez/
suppMaterialCVIU_17_288_v1.0.zip

$$N(v) = \begin{pmatrix}
0 & 0 & 0 & 1 & 0 & 0 & 0 & 0 & 0 & 0 & 1 & 0 & 1 & 0 & 0 \\
0 & -2 & 0 & 0 & 0 & 0 & -2 & 0 & -2 & 0 & 0 & 0 & 0 & 0 & 0 \\
0 & 2v & 0 & 0 & 0 & 0 & 2v & 0 & -2 & 0 & 0 & 0 & 0 & 0 & 0 \\
0 & 0 & 0 & 2v & 0 & 0 & 0 & 0 & 0 & 0 & 2v & 0 & -2 & 0 & 0 \\
0 & 0 & 0 & 0 & 2v & 0 & 0 & 0 & 0 & 0 & 0 & 2v & 0 & -2 & 0 \\
1 & 0 & 0 & 1 & 0 & 1 & 0 & 0 & 0 & 0 & 0 & 0 & 0 & 0 & 0 \\
-2v & 0 & 0 & -2v & 0 & 2 & 0 & 0 & 0 & 0 & 0 & 0 & 0 & 0 & 0 \\
0 & -2v & 0 & 0 & 0 & 0 & -2v & 0 & 2 & 0 & 0 & 0 & 0 & 0 & 0 \\
0 & 0 & -2v & 0 & 0 & 0 & 0 & -2v & 0 & 2 & 0 & 0 & 0 & 0 & 0 \\
v^2 & 0 & 0 & v^2 & 0 & -2v-1 & 0 & 0 & 0 & 0 & 0 & 0 & 0 & 0 & 0 \\
0 & 2v^2 & 0 & 0 & 0 & 0 & 2v^2 & 0 & -4v-2 & 0 & 0 & 0 & 0 & 0 & 0 \\
0 & 0 & 2 & 0 & 0 & 0 & 0 & 2 & 0 & 2 & 0 & 0 & 0 & 0 & 0 \\
0 & 0 & 0 & v^2 & 0 & 0 & 0 & 0 & 0 & 0 & v^2 & 0 & -2v-1 & 0 & 0 \\
0 & 0 & 0 & 0 & 2 & 0 & 0 & 0 & 0 & 0 & 0 & 2 & 0 & 2 & 0 \\
v^2-1 & 0 & 0 & 2v^2-2 & 0 & -2v-1 & 0 & 0 & 0 & 0 & v^2-1 & 0 & -2v-1 & 0 & 1
\end{pmatrix} \tag{B.1}$$

with $v = 2Z_{Rel}^2 - 1$.

$$H(Z_s) = \begin{pmatrix}
Z_s^2 & 0 & 0 & 0 & 0 & 0 & 0 & 0 & 0 & 0 & 0 & 0 & 0 & 0 & 0 \\
0 & Z_s^2 & 0 & 0 & 0 & 0 & 0 & 0 & 0 & 0 & 0 & 0 & 0 & 0 & 0 \\
0 & Z_s^2 & Z_s & 0 & 0 & 0 & 0 & 0 & 0 & 0 & 0 & 0 & 0 & 0 & 0 \\
-Z_s^2 & 0 & 0 & Z_s & 0 & 0 & 0 & 0 & 0 & 0 & 0 & 0 & 0 & 0 & 0 \\
0 & 0 & 0 & 0 & Z_s & 0 & 0 & 0 & 0 & 0 & 0 & 0 & 0 & 0 & 0 \\
0 & 0 & 0 & 0 & 0 & Z_s^2 & 0 & 0 & 0 & 0 & 0 & 0 & 0 & 0 & 0 \\
0 & 0 & 0 & 0 & 0 & Z_s^2 & Z_s & 0 & 0 & 0 & 0 & 0 & 0 & 0 & 0 \\
0 & -Z_s^2 & 0 & 0 & 0 & 0 & 0 & Z_s & 0 & 0 & 0 & 0 & 0 & 0 & 0 \\
0 & 0 & 0 & 0 & 0 & 0 & 0 & 0 & Z_s & 0 & 0 & 0 & 0 & 0 & 0 \\
0 & 0 & 0 & 0 & 0 & Z_s^2 & 2Z_s & 0 & 0 & 1 & 0 & 0 & 0 & 0 & 0 \\
0 & -Z_s^2 & -Z_s & 0 & 0 & 0 & 0 & Z_s & 0 & 0 & 1 & 0 & 0 & 0 & 0 \\
0 & 0 & 0 & 0 & 0 & 0 & 0 & 0 & Z_s & 0 & 0 & 1 & 0 & 0 & 0 \\
Z_s^2 & 0 & 0 & -2Z_s & 0 & 0 & 0 & 0 & 0 & 0 & 0 & 0 & 1 & 0 & 0 \\
0 & 0 & 0 & 0 & -Z_s & 0 & 0 & 0 & 0 & 0 & 0 & 0 & 0 & 1 & 0 \\
0 & 0 & 0 & 0 & 0 & 0 & 0 & 0 & 0 & 0 & 0 & 0 & 0 & 0 & 1
\end{pmatrix} \tag{B.2}$$

$$J(\mathbf{x}) = \begin{pmatrix}
0 & -4z & 4y & 0 & 0 & 0 & 0 & 0 & 0 & 0 & 0 & 0 & 0 & 0 & 0 \\
z & 0 & -x & -3z & 3y & 0 & 0 & 0 & 0 & 0 & 0 & 0 & 0 & 0 & 0 \\
0 & 0 & 0 & 0 & -3z & 3y & 0 & 0 & 0 & 0 & 0 & 0 & 0 & 0 & 0 \\
0 & 2z & 0 & 0 & -2x & 0 & -2z & 2y & 0 & 0 & 0 & 0 & 0 & 0 & 0 \\
0 & 0 & z & 0 & 0 & -x & 0 & -2z & 2y & 0 & 0 & 0 & 0 & 0 & 0 \\
0 & 0 & 0 & 0 & 0 & 0 & 0 & 0 & -2z & 2y & 0 & 0 & 0 & 0 & 0 \\
0 & 0 & 0 & 3z & 0 & 0 & 0 & -3x & 0 & 0 & -z & y & 0 & 0 & 0 \\
0 & 0 & 0 & 0 & 2z & 0 & 0 & 0 & -2x & 0 & 0 & -z & y & 0 & 0 \\
0 & 0 & 0 & 0 & 0 & z & 0 & 0 & 0 & -x & 0 & 0 & -z & y & 0 \\
0 & 0 & 0 & 0 & 0 & 0 & 0 & 0 & 0 & 0 & 0 & 0 & 0 & -z & y \\
0 & 0 & 0 & 0 & 0 & 0 & 4z & 0 & 0 & 0 & 0 & -4x & 0 & 0 & 0 \\
0 & 0 & 0 & 0 & 0 & 0 & 0 & 3z & 0 & 0 & 0 & 0 & -3x & 0 & 0 \\
0 & 0 & 0 & 0 & 0 & 0 & 0 & 0 & 2z & 0 & 0 & 0 & 0 & -2x & 0 \\
0 & 0 & 0 & 0 & 0 & 0 & 0 & 0 & 0 & 1 & 0 & 0 & 0 & 0 & -x \\
0 & 0 & 0 & 0 & 0 & 0 & 0 & 0 & 0 & 0 & 0 & 0 & 0 & 0 & 0
\end{pmatrix} \tag{B.3}$$

Fig. B.25. Detail of matrices $N(Z_{Rel})$, $H(Z_s)$ **and** $J(\mathbf{x})$.

References

Agrawal, A., Ramalingam, S., 2013. Single image calibration of multi-axial imaging systems, in: IEEE Conference on Computer Vision and Pattern Recognition (CVPR), pp. 1399–1406.

Agrawal, A., Taguchi, Y., Ramalingam, S., 2010. Analytical forward projection for axial non-central dioptric and catadioptric cameras, in: 11th European Conference on Computer Vision (ECCV), pp. 129–143.

Agrawal, A., Taguchi, Y., Ramalingam, S., 2011. Beyond alhazen's problem: Analytical projection model for non-central catadioptric cameras with quadric mirrors, in: IEEE Conference on Computer Vision and Pattern Recognition (CVPR), pp. 2993–3000.

Baker, S., Nayar, S.K., 2001. Single viewpoint catadioptric cameras. Springer-Verlag New York, Inc., Secaucus, NJ, USA.

Barreto, J., 2003. General Central Projection Systems: Modeling, Calibration and Visual Servoing. Ph.D. thesis.

Bazin, J.C., Demonceaux, C., Vasseur, P., Kweon, I., 2010. Motion estimation by decoupling rotation and translation in catadioptric vision. Computer Vision and Image Understanding 114, 254–273.

Bermudez-Cameo, J., Barreto, J.P., Lopez-Nicolas, G., Guerrero, J.J., 2014a. Minimal solution for computing pairs of lines in non-central cameras, in: 12th Asian Conference on Computer Vision (ACCV).

Bermudez-Cameo, J., Lopez-Nicolas, G., Guerrero, J.J., 2014b. Line-images in cone mirror catadioptric systems, in: 22th International Conference on Pattern Recognition (ICPR).

Bermudez-Cameo, J., Lopez-Nicolas, G., Guerrero, J.J., 2015. Automatic line extraction in uncalibrated omnidirectional cameras with revolution symmetry. International Journal of Computer Vision 114, 16–37.

Bermudez-Cameo, J., Saurer, O., Lopez-Nicolas, G., Guerrero, J.J., Pollefeys, M., 2017. Exploiting line metric reconstruction from non-central circular panoramas. Pattern Recognition Letters .

Caglioti, V., Gasparini, S., 2005. On the localization of straight lines in 3D space from single 2D images, in: IEEE Conference on Computer Vision and Pattern Recognition (CVPR), pp. 1129–1134.

Caglioti, V., Gasparini, S., Taddei, P., 2007a. Methods for space line localization from single catadioptric images: new proposals and comparisons, in: IEEE 11th International Conference on Computer Vision (ICCV), pp. 1–6.

Caglioti, V., Taddei, P., Boracchi, G., Gasparini, S., Giusti, A., 2007b. Single-image calibration of off-axis catadioptric cameras using lines, in: International Conference on Computer Vision (ICCV), pp. 1–6.

Chen, W., Cheng, I., Xiong, Z., Basu, A., Zhang, M., 2011. A 2-point algorithm for 3D reconstruction of horizontal lines from a single omni-directional image. Pattern Recognition Letters 32, 524–531.

Chum, O., Matas, J., 2005. Matching with prosac-progressive sample consensus, in: IEEE Conference on Computer Vision and Pattern Recognition (CVPR), pp. 220–226.

Gasparini, S., Caglioti, V., 2011. Line localization from single catadioptric images. International Journal of Computer Vision 94, 361–374.

Gonçalves, N., 2010. On the reflection point where light reflects to a known destination on quadratic surfaces. Optics letters 35, 100–102.

Gonçalves, N., Nogueira, A.C., 2009. Projection through quadric mirrors made faster, in: IEEE 12th International Conference on Computer Vision Workshops (ICCV Workshops), pp. 2141–2148.

Hartley, R.I., Zisserman, A., 2000. Multiple View Geometry in Computer Vision. Cambridge University Press, ISBN: 0521623049.

Isack, H., Boykov, Y., 2012. Energy-based geometric multi-model fitting. International journal of computer vision 97, 123–147.

Kanatani, K., 2015. Understanding geometric algebra: Hamilton, Grassmann and Clifford for Computer Vision and Graphics.

Lanman, D., Wachs, M., Taubin, G., Cukierman, F., 2006. Reconstructing a 3D line from a single catadioptric image, in: Third International Symposium on 3D Data Processing, Visualization, and Transmission, pp. 89–96.

López-Nicolás, G., Sagüés, C., 2014. Unitary torus model for conical mirror based catadioptric system. Computer Vision and Image Understanding 126, 67–79.

Miraldo, P., Araujo, H., 2014. Planar pose estimation for general cameras using known 3d lines, in: IEEE/RSJ International Conference on Intelligent Robots and Systems (IROS), pp. 4234–4240.

Miraldo, P., Araujo, H., Goncalves, N., 2015. Pose estimation for general cameras using lines. IEEE Transactions on Cybernetics 45, 2156–2164.

Perdigoto, L., Araujo, H., 2012. Reconstruction of 3D lines from a single axial catadioptric image using cross-ratio, in: 21th International Conference on Pattern Recognition (ICPR), pp. 857–860.

Perdigoto, L., Araujo, H., 2016. Estimation of mirror shape and extrinsic parameters in axial non-central catadioptric systems. Image and Vision Computing 54, 45–59.

Pinciroli, C., Bonarini, A., Matteucci, M., 2005. Robust detection of 3D scene horizontal and vertical lines in conical catadioptric sensors, in: Proc. 6th Workshop on Omnidirectional Vision.

Pottmann, H., Wallner, J., 2001. Computational line geometry. Springer.

Puig, L., Bermudez-Cameo, J., Sturm, P., Guerrero, J.J., 2012. Calibration of omnidirectional cameras in practice. a comparison of methods. Computer Vision and Image Understanding 116, 120–137.

Raguram, R., Chum, O., Pollefeys, M., Matas, J., Frahm, J., 2013. Usac: a universal framework for random sample consensus. IEEE Transactions on Pattern Analysis and Machine Intelligence 35, 2022–2038.

Selig, J.M., 2004. Geometric fundamentals of robotics. Springer Science & Business Media.

Sturm, P., Ramalingam, S., Tardif, J.P., Gasparini, S., Barreto, J., 2011. Camera models and fundamental concepts used in geometric computer vision. Foundations and Trends in Computer Graphics and Vision 6, 1–183.

Swaminathan, R., Wu, A., Dong, H., et al., 2008. Depth from distortions, in: 8th Workshop on Omnidirectional Vision, Camera Networks and Non-classical Cameras-OMNIVIS.

Tardif, J., Sturm, P., Roy, S., 2006. Self-calibration of a general radially symmetric distortion model. 9th European Conference on Computer Vision (ECCV) , 186–199.

Teller, S., Hohmeyer, M., 1999. Determining the lines through four lines. Journal of graphics tools 4, 11–22.

Ying, X., Zha, H., 2005. Simultaneously calibrating catadioptric camera and detecting line features using hough transform, in: IEEE/RSJ International Conference on Intelligent Robots and Systems (IROS), pp. 412–417.

Zhang, Q., Shen, X., Xu, L., Jia, J., 2014. Rolling guidance filter, in: European Conference on Computer Vision (ECCV), pp. 815–830.